Geometry and kinematics of the Cañones Fault and the effects of lithology on the distribution of strain within the Cañones Fault damage zone

---

A Thesis Presented to the Faculty of the

Department of Earth and Atmospheric Sciences

University of Houston

In Partial Fulfillment of the Requirements

for the Degree Master of Science

By

Kevin A. O'Keeffe

May 2014

Geometry and kinematics of the Cañones Fault and the effects of lithology on the distribution of strain within the Cañones Fault damage zone

Kevin A. O'Keeffe

APPROVED:

Dr. Michael A. Murphy (Advisor)

Dr. Alexander Robinson (Committee Member)

Dr. David E. Wolf (Committee Member)
Shell International Exploration and Production

Dr. Dan E. Wells
Dean, College of Natural Science and Mathematics

Geometry and kinematics of the Cañones Fault and the effects of lithology on the distribution of strain within the Cañones Fault damage zone

---

An Abstract Presented to the Faculty of the

Department of Earth and Atmospheric Sciences

University of Houston

In Partial Fulfillment of the Requirements

for the Degree Master of Science

By

Kevin A. O'Keeffe

May 2014

ABSTRACT

Understanding the structural history of a region is critical in the interpretation of fault system geometry and strain distribution. This study investigates deformation along the Cañones normal fault which marks the western boundary of the Rio Grande Rift in north-central New Mexico. Geologic mapping at a scale of 1:6,000 and structural reconstructions show that the Cañones fault formed in the forelimb of a west-vergent shortening-related monocline. Its footwall strata are sub-horizontal. Folded Jurassic strata in the hanging wall are eroded and unconformably overlain by Cenozoic rift deposits. The Cañones Fault and the monocline are sub-parallel. The amount of extension and shortening across the Cañones Fault and Laramide monocline decreases from south to north. Structural reconstructions indicate 170 meters of extension and 76 meters of shortening in the south, and 58 meters of extension and 16 meters of shortening in the north. Beyond termination of the monocline to the north, the trace of the Cañones fault trends nearly E-W and extension decreases to 42 meters. Although temporally separated, these structures are geometrically and spatially similar, suggesting Rio Grande Rift structures exploited Laramide structures.

Field mapping, fracture scanlines and structural modeling are used to investigate lithologic controls on fault damage zone attributes at the Cañones Fault in the Entrada Sandstone and overlying Todilto Limestone. These lithologies exemplify end-member type damage zones, deformation banded and fractured. Density of damage zone structures in the Todilto Limestone and the Entrada Sandstone reach background levels at nearly the same distance from the fault core (101-105 m), and are consistent with similar

data from other faults. Although the lithologic control on damage zone width is negligible, the distribution of fault damage zone structures differs by lithology. Deformation band and fracture distribution in softer rocks such as eolian sandstone and siliceous mudstones, tend to be clustered near the fault core and exponentially decay to background levels. Fracture distribution in more brittle lithologies such as limestone and porcelanite tends to be distributed throughout the damage zone with some clustering at the fault core ending abruptly at the outer margin of the fault damage zone.

TABLE OF CONTENTS

List of Figures

1. INTRODUCTION

1.1 Thesis Scope and Organization

The aim of this study was to characterize fault damage zone attributes with respect to lithology at the Cañones Fault located in north-central New Mexico near the town of Abiquiu; specifically the extent to which damage zone structures (fractures and deformation bands) extend from the fault core into the hanging wall and their density and distribution within the hanging wall damage zone. In addition, this study appraises inferred geometric and kinematic similarities between structures formed during Late Cretaceous-Early Tertiary Laramide contraction and those formed during Neogene Rio Grande Rift extension at a major basin bounding fault (The Cañones Fault) on the eastern margin of the Colorado Plateau in North Central New Mexico.

It has been inferred by other workers (Chapin and Cather 1994; Ingersoll 2001; Chapin and Seager 1975) that geometry and spatial relationships of structures formed during Neogene Rio Grande Rift extension have been influenced by older shortening related structures. To test this inference, this study focuses on two main sub-parallel structures found in the local study area (Figure 1). They are the southeast-dipping Cañones Fault and a west-vergent shortening-related monocline. Geologic mapping suggests that the Cenozoic Cañones Fault, formed in the forelimb of the shortening related structure that we interpret to be of Laramide age. This relationship was determined based on unconformity and cross-cutting relationships detailed in Chapter 3 (Cañones Fault and Laramide Monocline Geometry and Kinematics) of this manuscript. Structural

reconstructions carried out perpendicular to the two structures suggest that the Cañones Fault exploited pre-existing crustal weaknesses caused by the shortening related monocline.

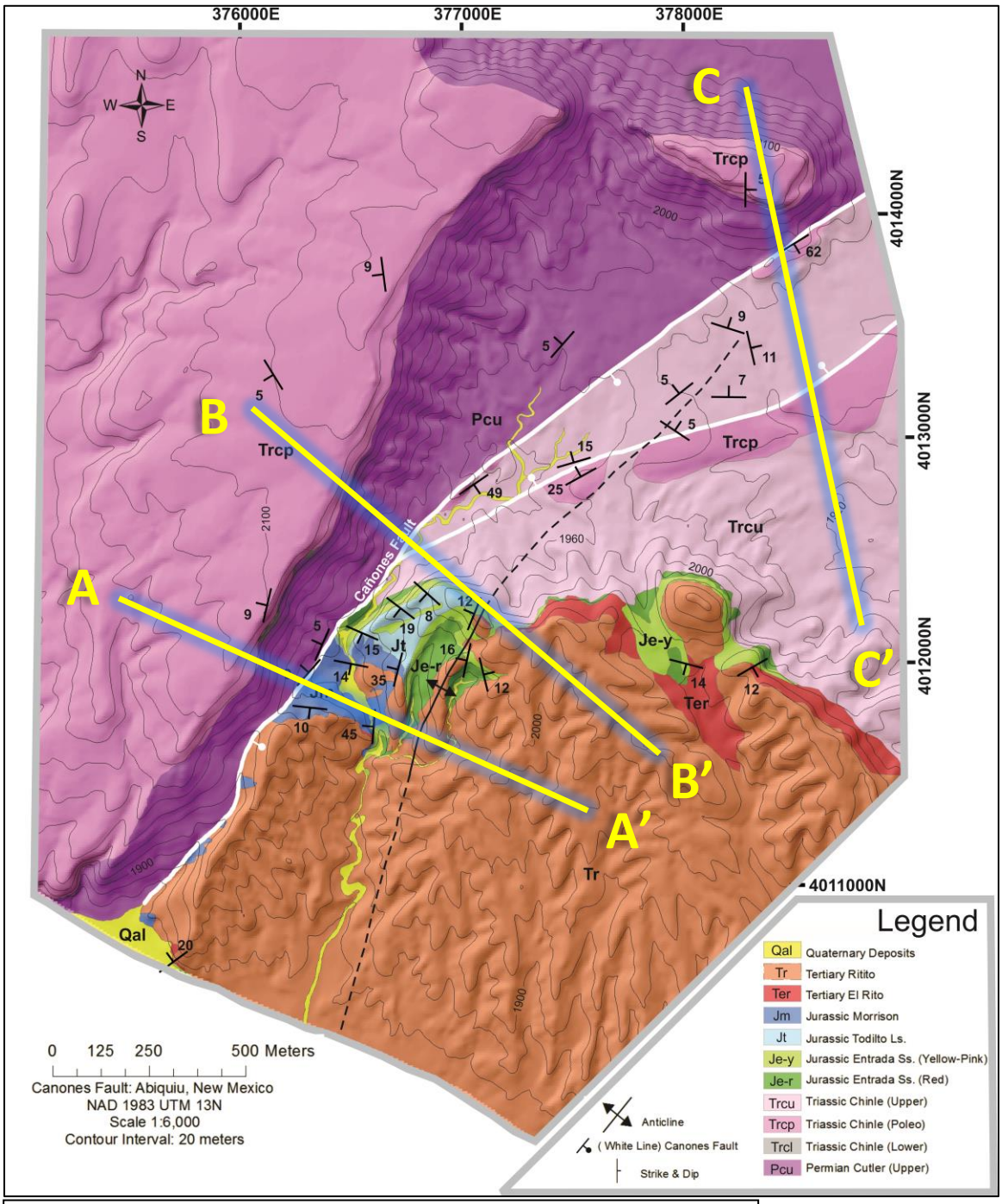

Figure 1. Geologic map of local study area along the Cañones Fault

Fault damage zones explored in this study are divided into a two end-member framework: (1) fractured and (2) deformation banded. Fractured fault damage zones have been observed to enhance the flow of fluids in subsurface petroleum reservoirs (Nelson 2000). Damage zones where deformation bands formed have been documented to act as barriers to subsurface fluid flow (Solum *et al.* 2010; Hesthammer *et al.* 2002; Fossen *et al.* 2003; Antonellini *et al.* 1999 and Lewis and Couples 1993). Damage zone end member type is highly dependent on lithology. Porous granular eolian and fluvial sandstone (Fossen et. al 2007; Berg and Skar 2005; Schueller *et al.* 2013), and carbonate grainstone (Tondi *et al.* 2005) are shown to host deformation-banded fault damage zones. More brittle dolomite, porcelanite (Eichhubl and Boles 1998), igneous (Faulkner *et al.* 2010 and Mitchell and Faulkner 2009) and limestone (Billie *et al.* 2003) lithologies are shown to host fractured fault damage zones. Although fault damage zones have been studied in a variety of lithologies by the afore-mentioned workers, a gap in understanding of the effect of lithology on the distribution and extent of deformation structures hosted by the fault damage zone still exists. This is because the previously mentioned studies were conducted at faults formed under differing stress conditions. Therefore, differing fault dips, fault slip directions, fault plane bends and asperities and differences in general fault cohesiveness can be expected, all of which will affect the distribution of deformation structures within the fault damage zone (Kim *et al.* 2004). Lithological effects on the distribution of strain and fault damage zone width are explored at a spectacular fault outcrop along the Cañones Fault where Permian rocks in the footwall juxtapose Jurassic Entrada Sandstone (deformation banded fault damage zone end-

member) and the Jurassic Todilto Limestone (fractured fault damage zone end-member) in the hanging wall (Figure 2).

Fault damage zones have been shown to be asymmetrical about the primary fault slip surface regardless of geological settings and on a range of scales (Aydin and Johnson 1978; Antonellini and Aydin 1995; Knott *et al.* 1996; Nelson *et al.* 1999; Fossen *et al.* 2007; Berg and Skar 2005; Du Bernard 2002; Flodin and Aydin 2004). Ferrill *et al.* (2011) suggests that faults nucleate in brittle lithology forming extensional fault propagation monoclines in deeper and more shallow sections. Then as the fault propagates to shallower levels through the monocline, damage zone asymmetry is concentrated in the hanging wall. As the fault propagates to depth, damage zone asymmetry is skewed toward the footwall. This assumption is based on a combination of modeling and field observations. The Cañones Fault is a basin-bounding fault surrounded by Laramide uplifts of Proterozoic igneous and metamorphic rock. Following Ferrill *et al.* (2011)'s logic, the Cañones Fault must have initiated in the more brittle crystalline rock and propagated upward through the Jurassic Entrada Sandstone and Todilto Limestone concentrating most of the off-fault damage in its hanging wall. This, along with the absence of the Entrada Ss. and Todilto Ls in the footwall, direct our damage zone study to the hanging wall of the Cañones Fault.

This study is a complete dataset including fault damage zone fracture and deformation band data and associated descriptive plots, regional and local geology and interaction between local structures that are spatially and kinematically similar, but temporally separated. It is organized in a manner which incorporates the Cañones Fault

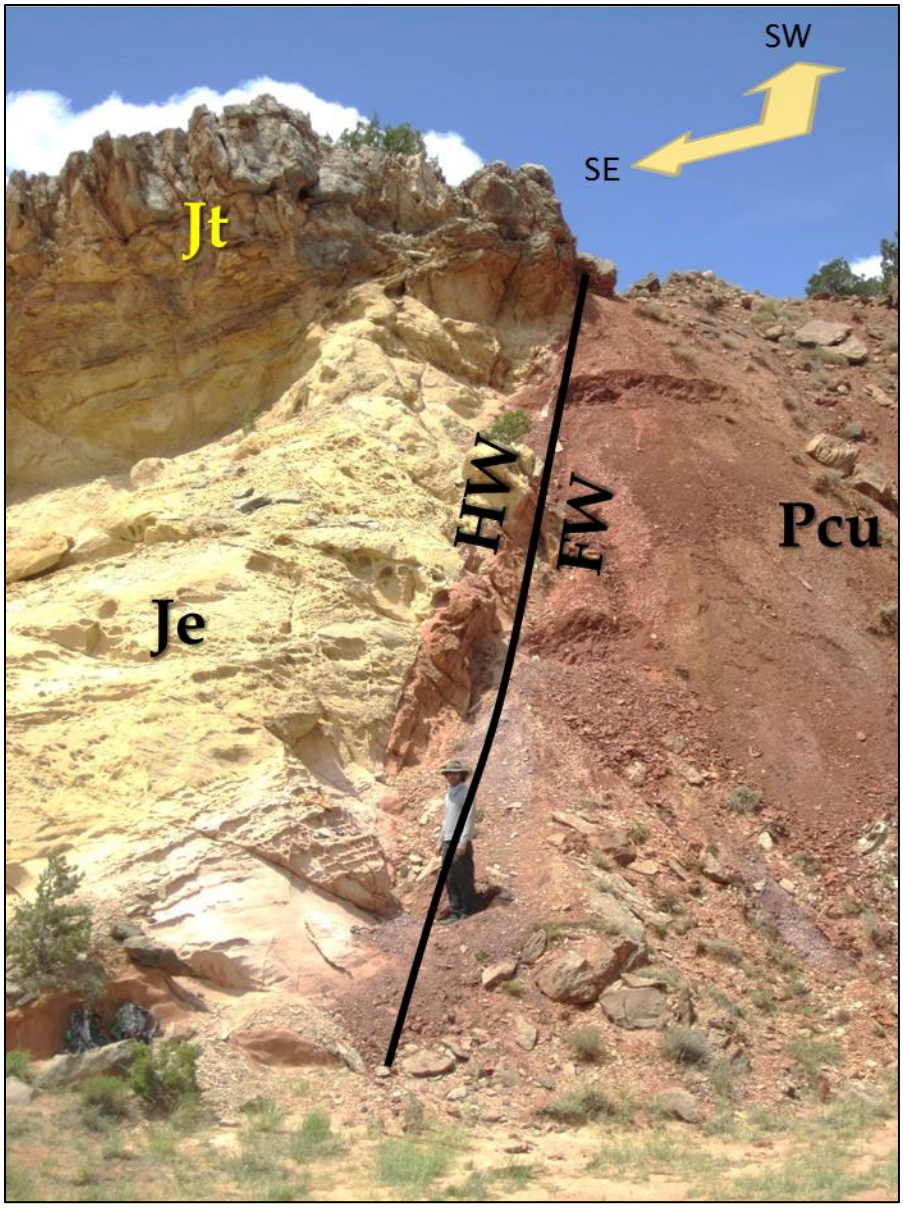

Figure 2. Field photograph showing outcrop of the Cañones Fault juxtaposing Permian Cutler Formation in the footwall and Jurassic Entrada Ss. and Todilto Ls. in the hanging wall.

damage zone into the context of regional and local geology, to elucidate any factors external to lithology that may control fault damage zone structure distribution and extent.

Studies of fault damage zones are important because these zones are known for hosting fractures and/or deformation bands, which can enhance or impede respectively, the flow of fluids in the earth's crust. Nelson (2000) maps marked increases in oil production near faults in Venezuela's La Paz field. In this field, fault damage zones containing an abundance of flow enhancing fractures allow economic levels of oil production in low porosity/permeability carbonate rock. The Gulfaks and Gulfaks Sør fields located in the North Sea produce from deformation-banded reservoirs. The two fields are separated by a major extensional fault and produce from the same age reservoir. The Gulfaks Field produces an average of 15,000 barrels of oil per day (bopd) and the Gulfaks Sør Field produces close to 1,700 bopd. In the Gulfaks Sør Field higher temperatures have been found to accelerate quartz precipitation and dissolution augmenting the fluid baffling effect of the deformation bands relative to those in the Gulfaks Field (Hesthammer 2002). Application of findings from this study may be carried over to petroleum reservoir or aquifer scenarios in which faulting may affect movement of fluids in the subsurface. These data can be used as input to reservoir models in faulted areas where subsurface predictions are limited by seismic data resolution and one dimensional well control.

1.2 Introduction to the Geology of North Central New Mexico

Along the eastern margin of the Colorado Plateau in north-central New Mexico, Late Cretaceous to Early Tertiary Laramide contraction overprinted by Neogene rift extension represent a prolonged period of foreland deformation in the North American Western Cordillera. Woodward (1974) divides this region into three primary physiographic

provinces based on differing styles of deformation, age and type of sedimentation: the Colorado Plateau, the Southern Rocky Mountains and the Rio Grande Rift.

The Colorado Plateau is a thick crustal block of relatively high relief that has not been deformed as severely as the surrounding terrains. Its eastern portion located in North-Central New Mexico, is divided into the Chama Basin and the San Juan Basin separated by the Gallina-Archuleta Arch (Figure 3). The Chama Basin is a broad synclinal feature that lies between the Gallina-Archuleta Arch and the Brazos Uplift. Basin geometry is elongate in the north-south direction about 10km long and at its widest point east-west is about 30 km. Structurally, the basin sits 457 meters below the highest point along the Gallina-Archuleta Arch and is 2,133 meters lower than the Brazos Uplift (Woodward, 1974). The southernmost part of the Chama Basin accommodates Late Paleozoic and Mesozoic sedimentary strata, while to the north Cenozoic sedimentary and volcanic rocks overlie these older strata (Smith *et al.*, 1961).

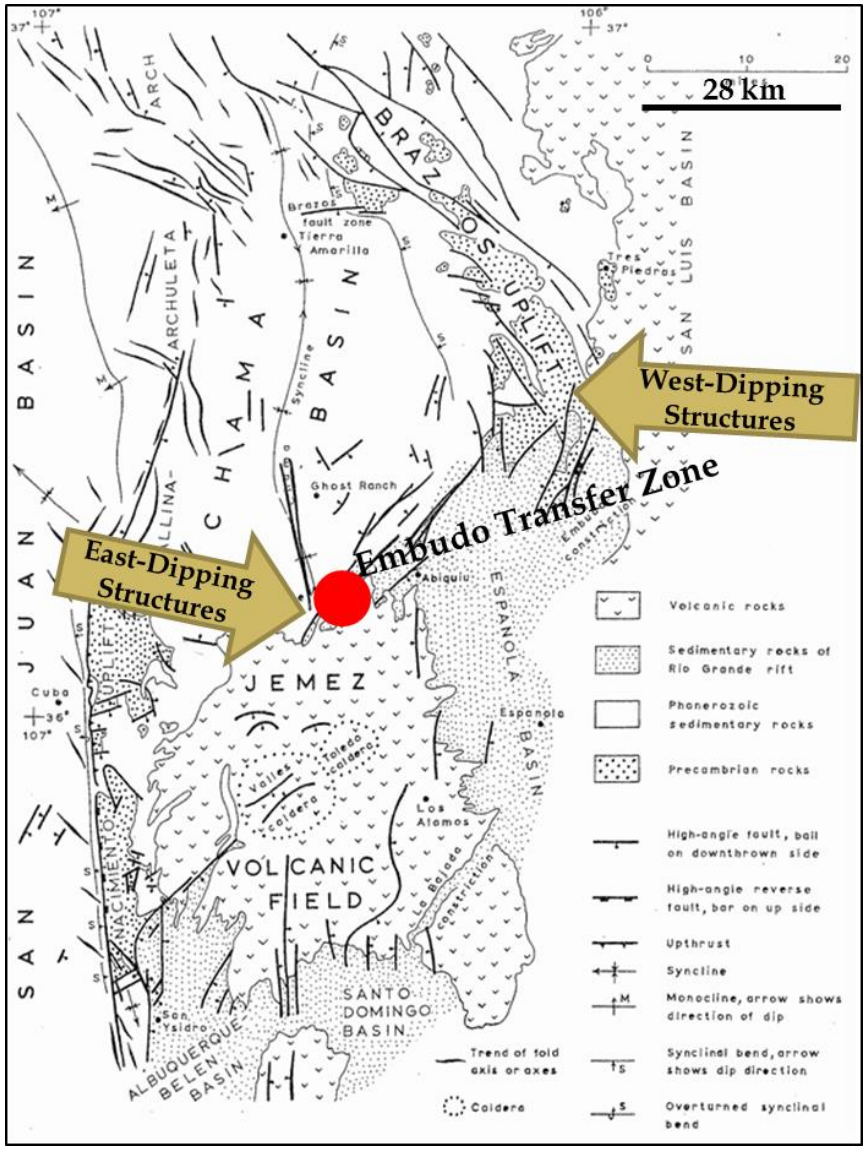

Figure 3. Simplified geologic map of North Central New Mexico (modified from Woodward 1974).

The northeastern margin of the basin is bound by steep, primarily west-dipping, faults that mark the boundary between the Brazos Uplift and the Chama Basin. The southeast margin of the Chama Basin is separated from the down-dropped, Rio Grande Rift related Espanola Basin by a set of northeast-striking extensional faults of Neogene age that dip primarily to the southeast. Along the western margin of the Chama basin lies the Gallina-

Archuleta Arch, a north trending, shortening related, monoclonal structure that separates the Chama Basin from the San Juan Basin. The monocline is a west-verging structure with the forelimb dipping steeply into the San Juan Basin to the west, whilst the back limb gently dips into the Chama basin to the east (Woodward, 1974). Structural relief is approximately 2600 meters between the Gallina-Archuleta Arch and the San Juan Basin which is slightly less than that between the Gallina-Archuleta Arch and the Nacimiento Uplift, which borders the eastern margin of the Colorado Plateau south of the Chama Basin (Woodward, 1974). The formation of the arch is dated at approximately 80 Ma which is synchronous with formation of the Nacimiento Uplift (Brister and Chapin, 1994; Cather, 2004). The San Juan Basin is an asymmetrical synclinal feature with an arc-shaped axis that is bowed to the northwest. It has a steep northern limb and a shallow southern limb and has a diameter of approximately 1600 km. The basin is bordered on its southeastern margin by the Nacimiento Uplift and the Gallina-Archuleta Arch borders the basin along its northeastern margin (Cather, 2004). Structural relief is estimated to be 3,048 meters between the Nacimiento Uplift and the San Juan Basin. This basin began as part of the Western Interior Basins associated with widespread tectonic loading from the Cordilleran thrust belt to the west between 95 and 80 Ma.

The Southern Rocky Mountains are the result of Late Cretaceous to Early Tertiary Laramide contractional deformation occurring on the eastern flank of the Colorado Plateau, and are divided into the Naciamento and the Brazos uplifts (Figure 3). The Brazos Uplift is a northwest-southeast trending structural feature that extends 80 kilometers in length and is about 40 km wide. It spans from northern New Mexico into southern Colorado. It is made up of primarily Proterozoic basement rocks covered in

areas by Tertiary volcanic and clastic rocks. The eastern margin of the uplift is bound by the Tusas-Picuris Fault, along lived feature resulting from multiple slip events dating back to about 1.2-0.8 Ga (Cather *et al.*, 2005). The southern portion of the uplift is highly segmented by Neogene extensional faulting associated with Rio Grande Rifting. Structural relief between the Brazos Uplift and adjacent basins of the Rio Grande Rift is estimated to be 3,658 meters (Shaffer, 1970). The Nacimiento Uplift is a north-south trending structural high covering an area approximately 80 km in length and 10-16 km in width. It is made up of east-dipping Proterozoic and younger rocks (Woodward, 1974). Faulting responsible for the Nacimiento Uplift are in general steeply east-dipping reverse faults that flatten near the surface where they are exposed (Woodward, 1987). A north-plunging faulted anticline is responsible for uplift of the northern portion of the Nacimiento Mountains that trends into the Gallina-Archuleta Arch (Woodward, 1974). Volcanic rocks of the Jemez Volcanic Field cover the east-dipping strata along the eastern margin of the Nacimiento Uplift. Kinematics of the faulting associated with the Nacimiento Uplift remain controversial. Some workers propose that dip-slip motion is primary while others suggest large amounts of strike slip.

The Rio Grande Rift, resulting from Neogene extension, overprints deformation associated with the southern Rocky Mountains and is divided into the Espanola Basin and the San Luis Basin (Figure 1) (Woodward, 1974). The Espanola Basin is a half graben that tilts down to the northwest that is elongate north to south covering an area 65-80 km in length and 30-65 km in width (Woodward 1974). The Northwest margin is bordered by major basin-bounding, southeast-dipping normal faults of Neogene age. The basin is filled primarily by syn-rift sedimentary rocks and earlier Eocene, Oligocene and Miocene

sedimentary rocks as well as volcanics from the nearby Jemez Volcanic Field to the south. These Espanola Basin rocks cover older Triassic and Jurassic rocks that were folded as a result of earlier tectonism. The San Luis Basin is basin inverted from a precursor Laramide uplift by Neogene Rio Grande Rift extension. It is elongate north to south covering an area 196 km in length and 119 km in width. Basin fill consists of Eocene and younger clastics and volcanics which sit directly atop granitic basement (Brister 1994). Primary tilt of the two basins are in opposite directions, Espanola Basin tilts to the west while the San Luis Basin tilts to the east (Manley 1984).

1.2.1 Laramide Orogeny

The term "Laramide" has been applied to both a tectonic event involving North American Cordilleran mountain building spanning late cretaceous to early Tertiary time, and a structural style describing basement-involved shortening structures (Spieker, 1946; Berg, 1962; Coney, 1972; Tweto, 1975 and Dickinson *et al*., 1988). The term will be used in this text primarily in relation to the former, Late Cretaceous to Early Tertiary compression affecting the western portion of North America. The Laramide Province spans from Mexico in the south, north to Montana and covers an area east west from Arizona into central New Mexico (DeCelles 2004). Structural style in the Laramide Province is dominated by moderate to high angle reverse faulting and back-thrusting which uplift Proterozoic crystalline and younger sedimentary and volcanic rocks. Interspersed between uplifts are primarily north-south trending basins that were the locus of Late Cretaceous to Eocene, fluvial, alluvial and lacustrine sedimentation (Yin and Ingersoll 1997 and DeCelles, 2004). The Laramide orogenic belt and its well inboard

location with respect to its paleo-arc are attributed to shallow subduction angle of the Farallon plate as it moved beneath North America (e.g., Dickinson and Snyder 1978).

1.2.2 Rio Grande Rift

The Rio Grande Rift is a Neogene-age extensional feature, extending from southern Colorado through New Mexico, and south into northern Mexico. It is the bounding feature between the deformed and topographically high Colorado Plateau and the low lying mid-continent plains of the United States. It has been affected by three significant geologic processes that have occurred through mid-late Cenozoic time. (1) The waning stages of Laramide contractional deformation gave way to Neogene extensional tectonism extending the Earth's crust from time of initiation of regional extension (~21 ma) to present. The most rapid phase of extension, sedimentation and stratal rotation spans 17 to 10 Ma (Ingersoll, 2001). (2) Volcanism, beginning approximately 35 Ma, was active sporadically until nearly 60 ka, most notably the Jemez Volcanic Field which is part of the non-time progressive Jemez Volcanic Lineament. (3) Erosional denudation that has helped shape the Rift's landscape. This is evident by the wide-spread removal of Mesozoic and early Cenozoic strata through Quaternary incision. The basins of the Rio Grande Rift are asymmetric half-grabens, averaging 50 km in width and 5-6 km of sediment thickness (Chapin and Cather 1994). The polarity of the normal faults bounding the basins changes from north to south across the Embudo transfer region. The normal faults are primarily east dipping in the southern basins and west dipping in the northern basins.

1.2.3 Pre-Existing Structure

In effort to adequately describe the geometrical similarity of temporally separated structures in North Central New Mexico, i.e. those related to Laramide shortening and those from Neogene extension, it is relevant to understand geometries and kinematics of more ancient underpinning tectonism. It is observed in this study and by other workers (*e.g.*, Chapin and Cather, 1994; Ingersoll, 2001; Chapin and Seager, 1975; Karlstrom *et al.*, 1999)) , that although temporally separated, many post-dating overprinting structures are geometrically and kinematically similar to, or affected by those structures formed

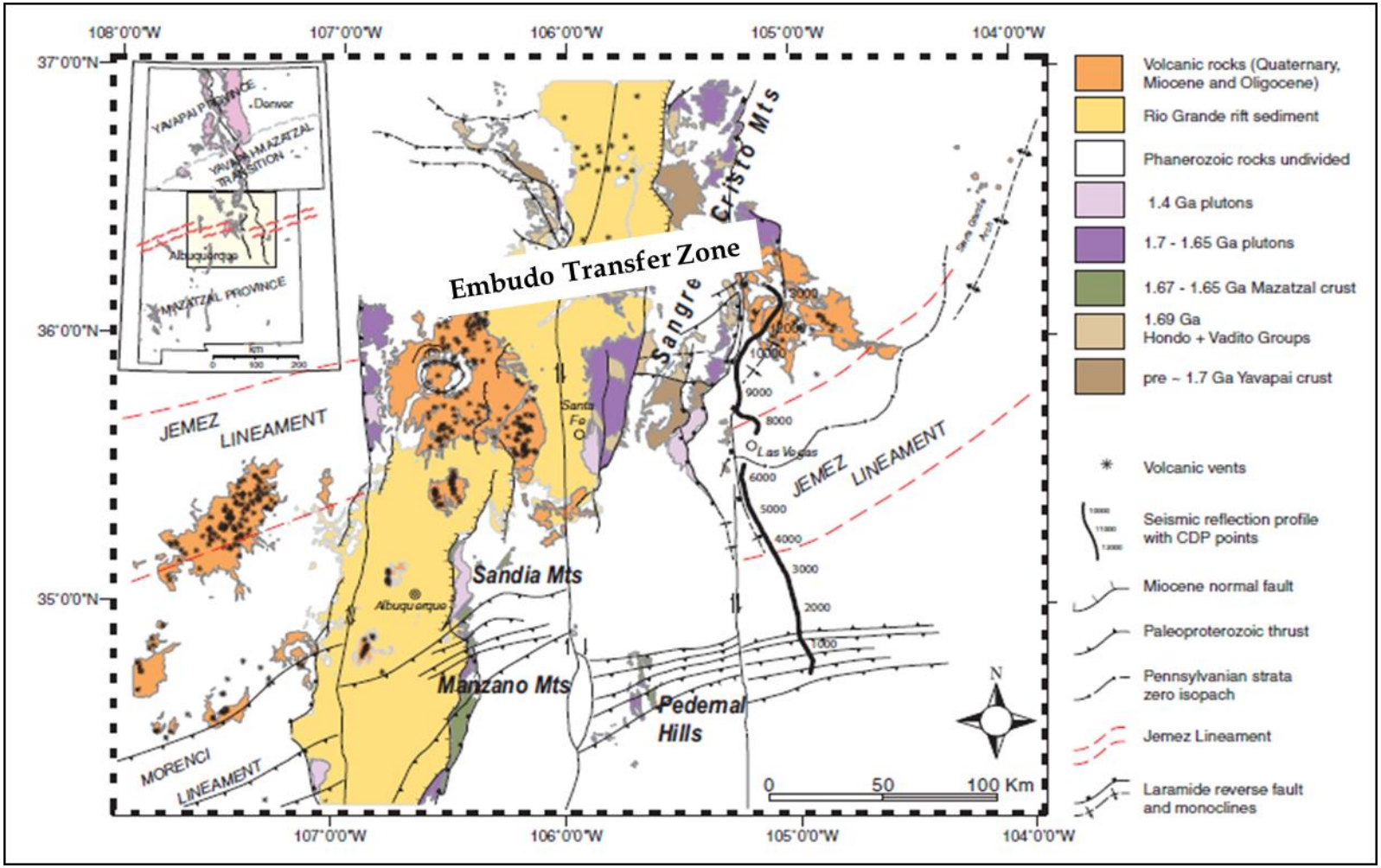

Figure 4. Simplified geologic map showing geometry of pre-existing structures and their spatial relationship to younger structures in North Central New Mexico (modified from Magnani et. al. 2004).

by earlier tectonism throughout north-central New Mexico. Present-day structural trends have been shown to exist since the age of the Ancestral Rocky mountains (Karlstrom *et al.*, 1999) where north-south trending structures are offset in the area of the present day Embudo transfer. Magnani *et al.* (2004) and Karlstrom and Daniel (1993) argue that the Jemez Lineament is the surface expression of a long lived volcanic and tectonic boundary inherited from suturing of the Mazatzal accreted island arc terrain and the Yavapai proto-North American craton (Figure 4) (1.68-1.65 Ga). Volcanic activity along the lineament is not time progressive. Meaning that older volcanism did not occur at one end of the lineament and progressively young away from the older volcanism to the termination of the lineament. Volcanism began in the central portion of the Lineament at 13.2 Ma, the southwest end around 9.8 Ma and the northeast end about 8.2 Ma. Just east of Colorado Plateau margin, along the surface trace of the Jemez Lineament, lies the Jemez Volcanic Field containing the Valles Caldera and the Toledo Caldera. This volcanic field marks the southwestern most edge of the Embudo Transfer fault trend, across which, the fault polarity reverses. Structures associated with Laramide shortening are primarily west-vergent east-dipping south of the transfer and primarily east vergant, west dipping north of the transfer. Likewise, structures associated with Rio Grande Rift extension dip primarily to the east south of the transfer, and north of the transfer structures dip primarily west (Figure 3).

1.2.4 Cañones Fault

The Cañones Fault zone, located in north-central New Mexico, near the town of Abiquiu, is the focus of this study (Figure 1, 5, and 13). It is the western most bounding fault of

the Rio Grande Rift, and marks the boundary between the Espanola Basin and the Chama Basin portion of the Colorado Plateau, thus marking the boundary between the Rio Grande Rift and the Colorado

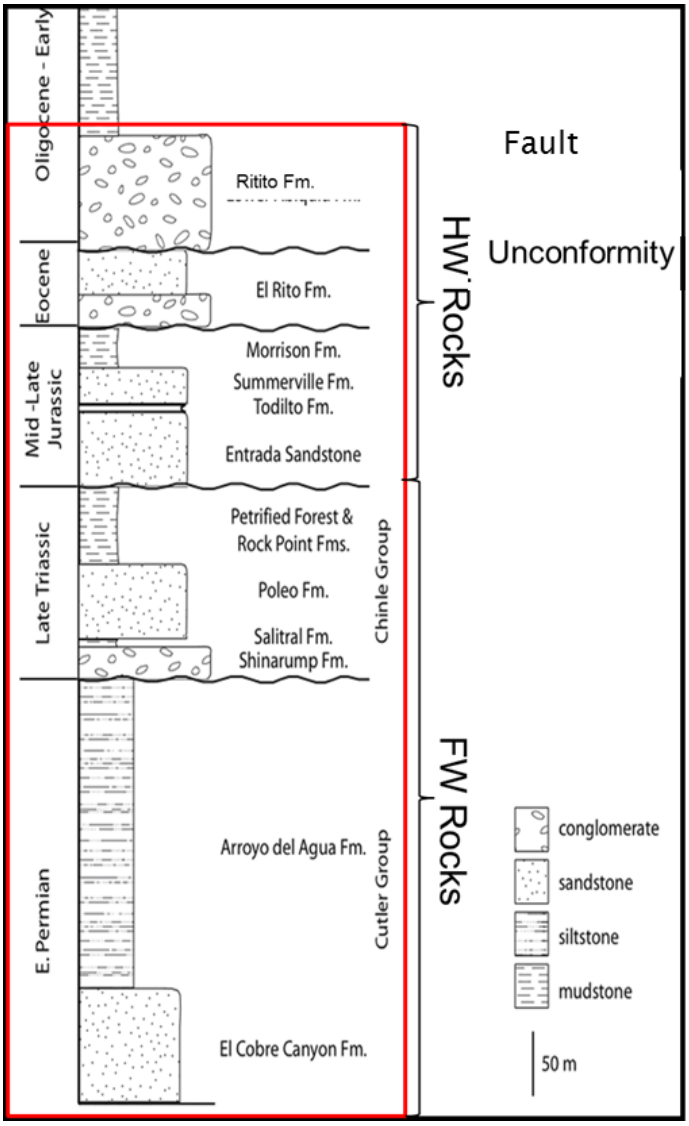

Figure 5. Stratigraphic chart of rock units in local study area (within red line) (modified from Kempner et. al. 2007).

Plateau. It cuts Mesozoic and Cenozoic strata of varying lithology along strike (Figure 5). Its footwall strata are sub-horizontal. In the hanging wall rocks are folded into a west-

verging shortening-related monocline. The fault plane strikes an average of N33°E and has an average dip of 68°SE. To the north, fault strike changes to east-west, and splays develop in the form antithetically-dipping faults. Slickenlines have average rakes of 78.8°NE and 73.5°NE, suggesting a minor component of right-lateral strike-slip accompanying an otherwise primarily dip-slip sense of motion. According to Gonzalez and Dethier (1991), the Cañones Fault zone offsets the ~8 Ma Lobado Basalt flow to the south by 570 meters. The younger ~3 Ma El Alto basalt flow crosses the fault trace, and shows no offset. Therefore, based on the topographic relations between the basalt flows, the minimum slip rate of the fault is calculated to be 570m/5m.y. (0.011 in cm/yr).

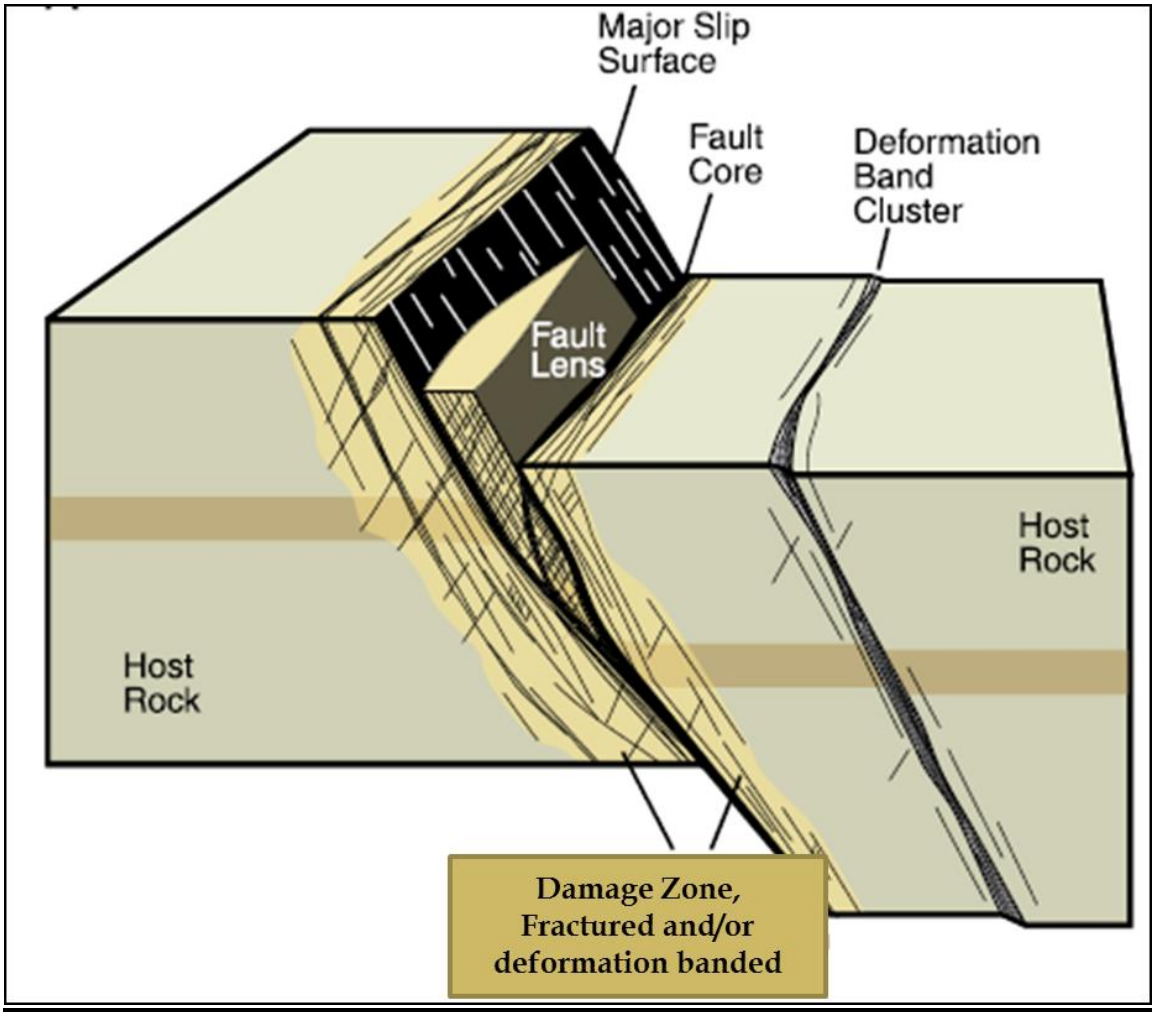

Figure 6. Cartoon diagram of fault zone anatomy observed at varying scales (modified from Torabi *et al*. 2013).

1.3 Fault Anatomy

Fault zones can be divided into three basic architectural components, which include the deformation-hosting rock, the fault core which accommodates the majority of the faults displacement, and the fault-damage zone which is the zone of intensified deformation enveloping the fault core (Figure 6). These fault-zone elements can be host to a variety of

structural elements (*e.g*., fractures, deformation bands, minor slip surfaces, fault core lenses, fault breccia) depending upon the mechanical properties of the deformation hosting rock (Braathen *et al.,* 2009).

1.3.1 Fault Core

The fault core is the basic component of a fault zone along which most of the faults displacement is accommodated (Figure 6). It can be host to cataclastic fault rock lenses, lenses of host rock, fractures and discrete slip surfaces. Key factors that control the development and geometry of fault core lenses include orientation of the principal fault plane with respect to principal stresses, magnitude of principal stresses, lithology of the deformation hosting rock and bulk fault displacement (Lindanger *et al.,* 2007). Lindinger *et al.* (2007) shows that there is a decrease in lens dimension with increasing fault displacement. A single fault core can vary in width along the fault plain, likely as a function of lithology and fault offset.

1.3.2 Fault Damage Zones

Fault-damage zones are areas of intensified deformation surrounding a fault core and extending a certain distance from the fault core into the hosting rock unit (Figure 6). They are characterized by fractures and deformation bands of different types and scales, joints and minor slip surfaces. Damage zones are by-and-large observed in field studies to be either predominantly fracture bearing (Billi *et al.,* 2003; Faulkner *et al.,* 2010; Mitchell & Faulkner, 2009; Savage *et al.,* 2010), or primarily dominated by deformation bands (Fossen, 2000; Beach *et al.,* 1994; Berg and Skar, 2005; Fossen *et al.,* 2007; Antonellini

and Aydin, 1995; Antonellini and Aydin, 1994; Du Bernard *et al.*, 2002; Knott *et al.*, 1996; Fowles and Burley, 1994) depending on the deformation hosting lithology. Fracture dominated damage zones typically occur in relatively more brittle and less granular material such as limestone, shale and crystalline rocks.

Deformation bands are defined by Aydin and Johnson (1978) as narrow, tabular zones of displacement, compaction, and/or cataclasis and are a product of stress acting upon porous material, such as eolian sandstone and carbonate grainstone. Deformation bands are different from faults and fractures as they do not exhibit a discrete fracture or slip surface, but similar to faults and fractures in that they are preferentially oriented with respect to maximum stress field. There are three main types of deformation bands (Figure 7): (1) Dilation bands (Figure 7c), which exhibit a volumetric change in the rock with zero shear, and can be host clay minerals and) (2) Disaggregation bands (Figure 7b) which result from localized volumetric strain and exhibit granular flow involving grain rolling, sliding and general reorganization, and in some cases simple shearing, and occur in areas affected by minimal amounts of effective stress, and (3) Cataclastic bands (Figure 7a) which are the product of rock volume decrease, are characterized by grain crushing, abrasion and/or cataclasis and many times are accompanied by simple shearing (Aydin *et al.*, 2006). As stated above, deformation bands have been observed to act as baffles to fluid flow in subsurface petroleum reservoirs. Their degree of fluid baffling is linked to their deformation mechanism, particularly the degree of cataclasis, dissolution, and phyllosilicate content.

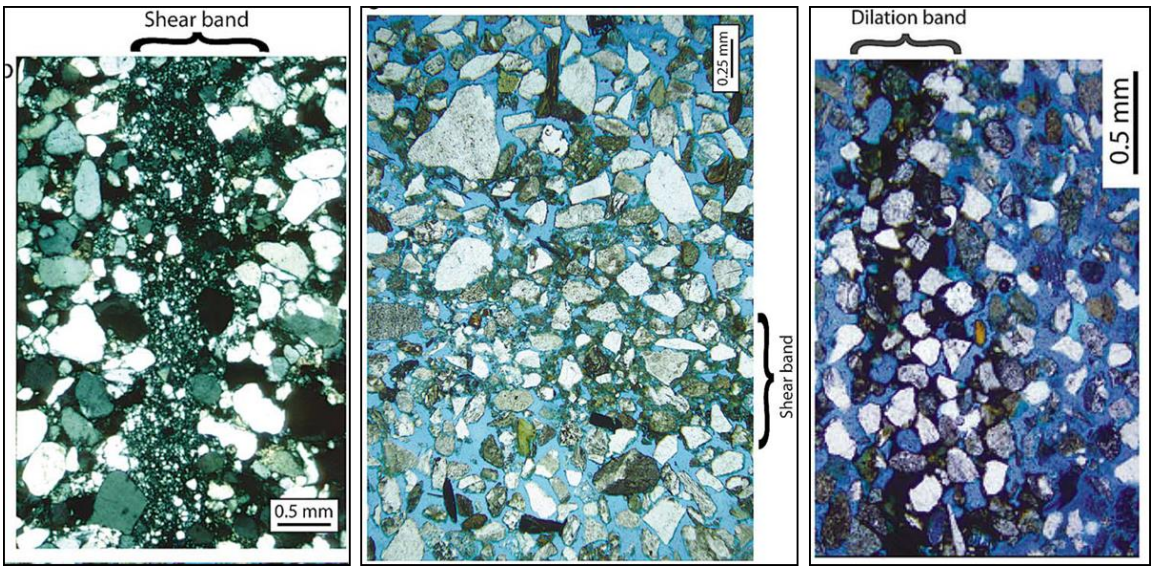

Figure 7 a, b & c. Deformation bands in thin section. a. Cataclastic shear band, b. Shear band with grain reorganization and compaction, but minor to no cataclasis, c. Dilation band showing disaggregation of grains and introduction of phyllosylicate mineral (modified from

Torabi (2007) shows up to four orders of magnitude reduction in permeability for cataclastic bands and deformation bands affected by dissolution. Deformation bands with phyllosilicate minerals have been shown to reduce permeability by up to two orders of magnitude (Torabi, 2007). On the "macro"-scale, deformation bands are strain-hardening features occurring in granular rock that have been observed as single tabular structures or as an aggregate or cluster of many deformation bands and are more resistant to weathering processes than the surrounding rocks (Figure 8).

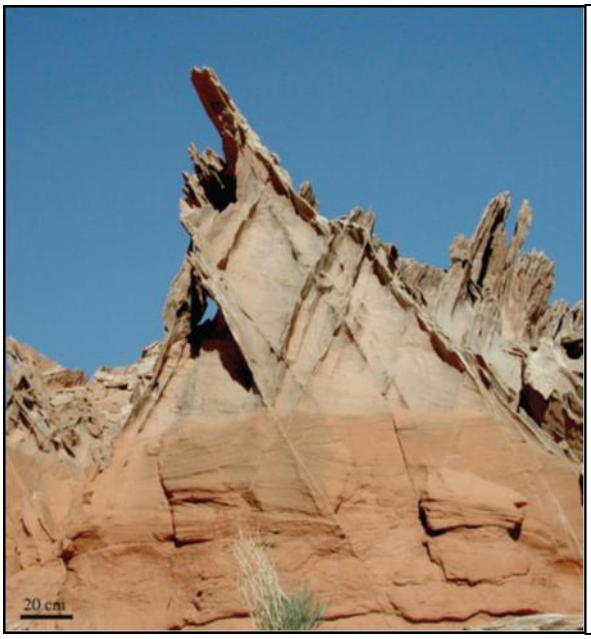

Figure 8. Field photograph showing conjugate deformation bands in the Entrada Sandstone. Note the resistance of the deformation bands to weathering relative to surrounding host rock (from Fossen et. al. 2007).

Fractures are cracks formed in brittle portions of the Earth's crust where stress causes loss of cohesion along weakened planes. They provide subsurface fluid conduits for aquifers and petroleum reservoirs. There are three main modes of fracturing: mode 1 (open mode) fractures involve the separation of rock by an open crack formed normal to the direction of extensional stress, mode 2 (sliding mode) fractures are caused by shear stress working perpendicular to the fracture plane and mode 3 (tearing mode) fractures are formed by shear stress acting parallel to the fracture plane. Fractures can be different modes at different times as principle stress directions change through time (Figure 9). When fractures are in open mode (mode 1), fluids are readily passed through them. If they are connected, they can act as the primary means for subsurface fluid flow. Veins are formed in open mode fractures that are filled with mineral precipitates. Several stages of mineral precipitation can occur in a single vein recording the fracture's opening history. When fractures are in mode 2 or mode 3 (shear fractures) fluid conduit action is at a minimum.

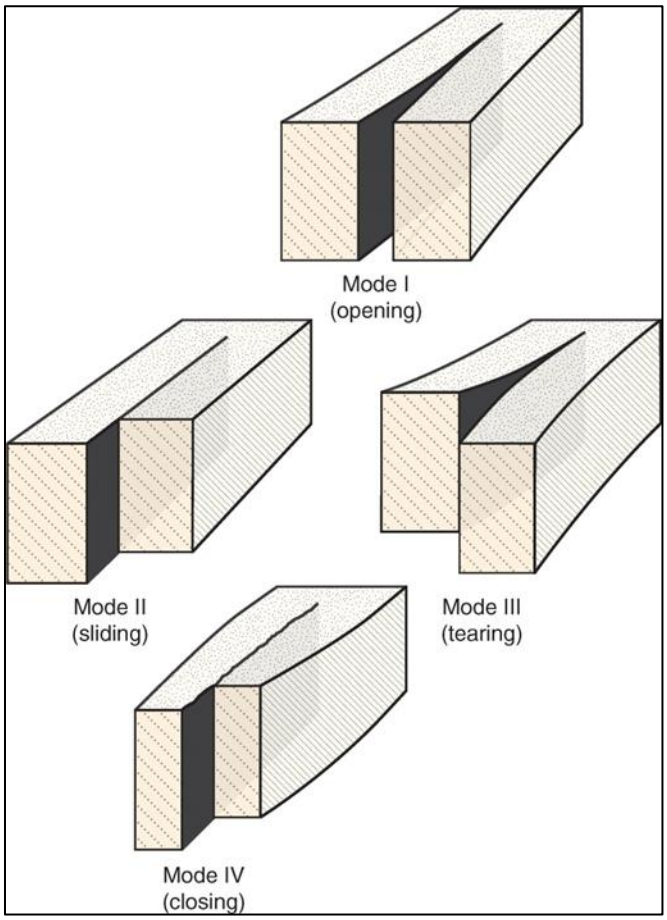

Figure 9. Diagram of fracture modes: Open mode 1, shear mode 2 sliding, shear mode 3 tearing, and closing mode 4. (From Fossen 2010)

1.3.3 Host Rock

Host rock or protolith in this case is the once pristine rock facies that accommodates faulting and associated damage. Host rock lithology can have profound effects on fault dips, type of off fault damage that occurs and the distribution of that damage throughout the fault damage zone.

1.4 Fault Damage Zone Formation

Fault damage zone is defined in Kim *et al.* (2004) as the volume of deformed wall rocks around a fault surface that result from the initiation, propagation, interaction and build-up of slip along faults. Despite differences in fault type and lithology present, general consensus is that damage zone formation results from three main processes: (1) Strain build-up prior to fault initiation, , (2) Fault tip propagation and (3) Fault displacement accumulation (Mitchell & Faulkner, 2009; Faulkner *et al.*, 2010; Billi *et al*., 2003; Kim *et al.*, 2004; Shipton and Cowie; 2003; and others). Controls on the formation of fault damage zones are interpreted to be fault plane dips, asperities or bends in the fault plane, bedding dips relative to the fault slip direction and lithology (Kim *et al.*, 2004).

It has been demonstrated theoretically, experimentally, and observed in field studies that faults are formed by the coalescence of many tensile microscopic and macroscopic cracks in the Earth's crust (Brace and Martin, 1968; Brace *et al*., 1966; Engelder, 1974; Healy *et al.*, 2006; Lockner *et al*., 1991; Paterson and Wong, 2005; Peng and Johnson, 1972; Mitchell and Faulkner, 2009; Billi *et al.*, 2003). Billi *et al.* (2003), in a field study, showed that continued degradation of fracture-induced lithons into condensed areas of fracture formed lineations oriented in the optimum-failure direction for strike-slip and extensional faults marks the transition from initial damage-zone formation to fault core. Similarly, Shipton and Cowie (2001) found that faulting in porous sandstone occurs as the coalescence of many deformation bands in a given area that form prior to a measurable through-going slip surface.

Fracture and deformation banding formed due to fault propagation occur in the volume of rock located at the tips of faults where initial displacement is at zero. Cowie and Scholz (1992) argue that the rock volume located at the fault tips will experience the highest stress concentration even more intense than stress resulting from subsequent slippage. As the fault tip migrates it will leave in its wake a damaged zone of fractures and/or deformation bands depending on damage zone end-member type. In this mode of damage zone formation, the size of the damage zone is determined by the magnitude of stresses surrounding the fault tip as it propagates (Cowie and Scholz, 1992; Scholz *et al*., 1993; Scholz and Lawler, 2004). Fractures and deformation bands occurring in the fault tip damage zone can be expected to trend at high and low angles to the fault plane depending on whether they are located in the tensile or compressive region of the fault tip respectively (Mitchell and Faulkner, 2009).

The majority of fault damage zone fractures and deformation bands are attributed to accumulation of slip on the primary fault surface (Schultz, 1987). Chester (2004) proposed that relict damage due to fault-tip propagation may be overshadowed by damage-zone structures formed during fault-slip accumulation. In addition, fault slip rates have been shown to be non-uniform along a single fault surface by Shipton and Cowie (2003), which may be expected to be recorded in the form of increased fracture or deformation band densities in the fault damage zone.

It has been demonstrated in fractured fault damage zones that once faults reach a certain amount of throw, propagation of the fault damage zone into surrounding host rock will subside Micarelli *et al.,* 2006 and Faulkner *et al.,* 2010). The optimum amount of throw

at which this occurs is related to the onset of cataclastic behavior along the primary fault slip surface of small (1-5 meter throw) faults according to Micarelli *et al.* (2006). Similarly, Faulkner *et al.* (2010) found that after a few hundred meters of displacement along large offset (35-5000 meters) strike-slip faults, damage-zone growth rate begins to decrease. At certain displacements, slip and deformation are observed to have become more concentrated on the primary fault slip surface slowing the damage zone growth rate (Micarelli *et al*., 2006 and Mitchell and Faulkner, 2009). This relates to degree of cohesion on a fault plane relative to slip. Theoretically, a perfectly frictionless fault will have no damage zone.

Fault damage zones have been observed to be asymmetric around the primary fault slip surface in most studies regardless of geological settings and on a range of scales (Aydin and Johnson, 1978; Antonellini and Aydin, 1995; Knott *et al.,* 1996; Nelson *et al.,* 1999; Fossen *et al.,* 2007; Berg and Skar, 2005; Du Bernard, 2002; Flodin and Aydin, 2004; Ferrill *et al.,* 2011). Asymmetry is commonly divided between the hanging wall and footwall damage zones. Common observations are that asymmetry is skewed heavily toward the hanging wall damage zone in extensional settings (Du Bernard, 2002; Berg and Skar, 2005; and others). Still, there are documented cases where damage occurs primarily in the footwall (Doughty, 2003; Ferrill *et al.,* 2011). Fault damage zone asymmetry has been proposed by Ferrill *et al.* (2011) to be controlled by fault nucleation and propagation. They show, that in a layered sequence of sedimentary rocks, faults will initiate in the most brittle layers at high dip angles forming extensional fault monoclines in over and under lying rocks. Then as the fault propagates upward at shallower dips the hanging wall is expected to accommodate most of the off-fault damage. Conversely, as

the fault propagates downward at more shallow dip the footwall is expected to collect most of the off-fault damage.

2. METHOD

A variety of geological data collection methods and analysis were used in this study. Geologic maps at varying scales are used to identify spatial relationships between structures at regional and local scales. Cross section construction and line length restoration methods were used to gain an understanding of subsurface fault and fold geometries and amount of deformation. Scanlines method of fracture and deformation band data collection were used to obtain an understanding of the distribution of structures with in the Cañones Fault damage zone. Data plots were used to analyze and exhibit the findings from mapped and scanline data. Data collection was focused in the area where the following rock units are present. Stratigraphic column from Kempner *et al*, 2007 (Figure 5):

2.1 Stratigraphic Units

Pcu- Arroyo del Agua Formation- This Early Permian unit (Figure 12) forms the upper part of the Cutler Group, which was divided into two distinct stratigraphic units, the Arroyo del Agua and the El Cobre Canyon Formations, by Lucas and Krainer 2005. This dominantly orange formation consists of many thick siltstone slope formers, interspersed with thin units of sandstone that are resistant to weathering. The sandstones are generally arkosic and display trough-crossbedding (Kempter *et al.*, 2007). It is easily differentiated from the underlying El Cobre Canyon Formation by its orange color and lack of thick cliff-forming sandstones. Only the Arroyo del Agua Formation is exposed at the study

site and surrounding area. For mapping purposes Permian rocks are undifferentiated and named under a single moniker Pcu (Permian Cutler Formation).

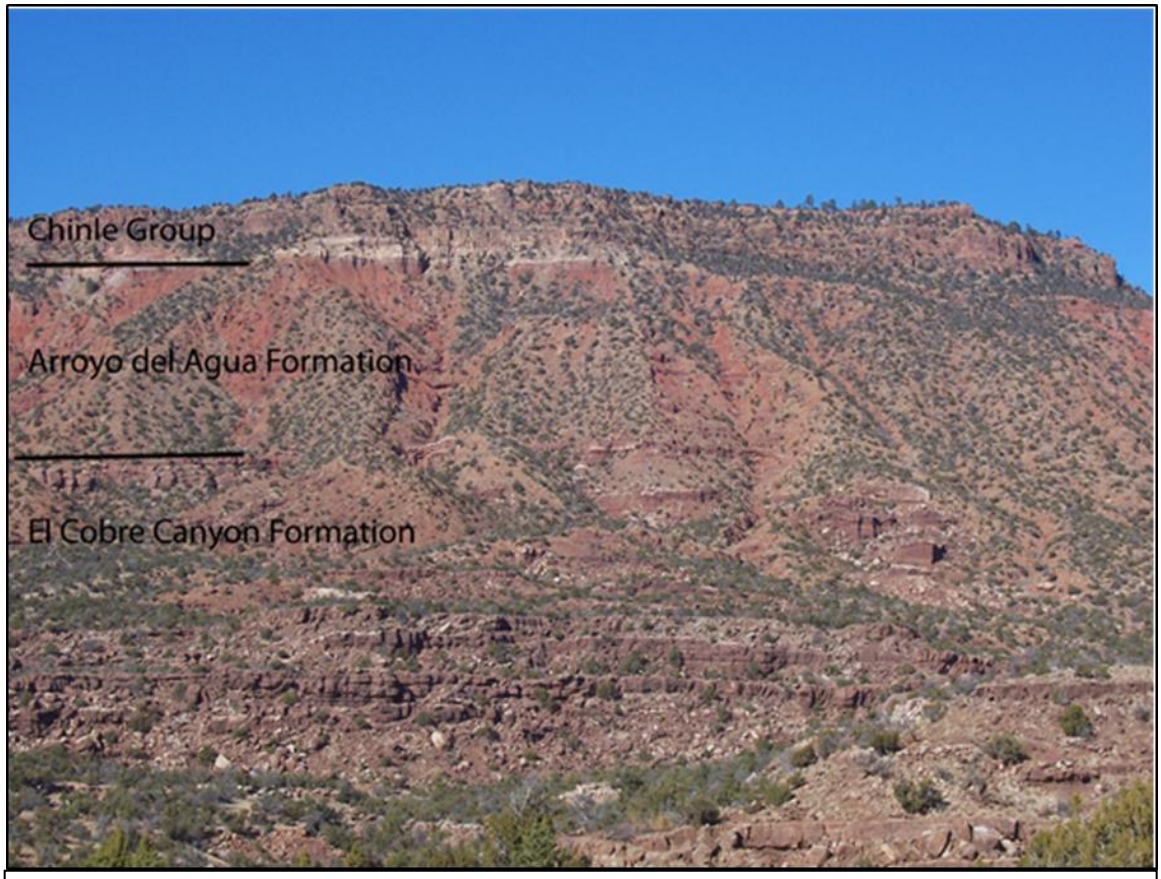

Figure 10. Photograph of northern wall of Cobre Canyon in the study area. The wall forms the footwall of the Cañones Fault.

TRcp- Chinle Group- Triassic Poleo Formation (Figure 12) is the middle unit of the Chinle Group. It forms prominent cliffs of cross-bedded sandstone. It is brown to gray to yellow medium to fine grained micaceous quartzos sandstone. Contact between the Poleo Formation and the underlying Permian rocks is sharp while a gradational contact exists between the Poleo and the overlying Upper Chinle Formation. The Poleo measures 41 meters thickness in the field area (at Abiquiu Dam) (Kelly *et al.*, 2005).

TRcu- Chinle Group- This Triassic Upper Chinle stratigraphy (Figure 12) includes two main formations which are not subdivided for the purposes of this study, but are lumped together as TRcl. These are the Rock Point Formation and the Petrified Forest Formation. The Rock Point Formation is reddish-brown to gray-red siltstone and fine grained sandstone. It forms slopes up to 70 meters thick (Lucas *et al.,* 2003). The Petrified Forest Formation is divided into two members: the basal Mesa Montosa Member that consists of red-brown laminated sandstone and the upper Painted Desert Member composed of red-brown mudstone. The formation as a whole is 200 meters thick (Kelly *et al.,* 2005).

Je- Entrada Sandstone- The Jurassic Entrada Sandstone (Figure 2) is an eolian deposited very-fine to medium grained quartzose sandstone. It is well sorted and moderately indurated. The Entrada Sandstone forms cliffs 60 to 67 meters thick that display a color scheme of red at the base, pink in the middle and yellow at the top (Kelly *et al.,* 2005). Ripple laminations as well as large scale dunal trough crossbedding are present along with deformation banding (Kempter *et al*., 2007). It has been determined by Lucas *et al.* (2005) that only the Slick Rock Member of the Entrada is present at the study site and surrounding area.

Jt- Todilto Formation- The Jurassic Todilto Formation (Figure 2) is a non-marine or saline-paralic deposited limestone that is high in organic content and lacks bioturbation or wave formed features (Berglof, 2003). It is thinly laminated at the base (millimeter scale laminations) locally microfolded and contorted, and more massive near the top. Its exact age middle Callovian is based on fossil evidence collected by Lucas (1985). In the study

area the Todilto varies in thickness up to 5 meters. The Todilto is bound by unconformities at its top and base. It overlies the Entrada Sandstone and is just below the Jurassic Morrison Formation (Kempter *et al*., 2007).

Jm- Morrison Formation- The Morrison Formation is divided onto the Jackpile Sandstone and the Brushy Basin Member (Kelly *et al.*, 2005). Only the Brushy Basin Member of the Morrison Formation is present in the field area. This unit consists of an interbedded base of mudstone and trough-crossbedded sandstone that is up to 8 meters thick. Toward the top it is a variegated green to reddish orange and in some places dark reddish brown siltstone and mudstone with significant bentonite content (Kelly *et al.*, 2005). This unit is on the order of 40 to 70 meters thick (Kempter *et al.,* 2007).

Ter- El Rito Formation- The Eocene El Rito Formation (Figure 11) underlies the Ritito Formation (formerly lower member of the Abiquiu Formation) and unconformably lies atop of Cretaceous Mancos Shale or Dakota Sandstone. In the study area, it unconformably overlies the Jurassic Morrison Formation. It consists of Proterozoic granite and quartzite pebbles to cobbles in an orange-red to brick-red, hematitic, micaceous silt to sand matrix. Locally, the 2 to 10 meter thick basal conglomerate section is made up of Proterozoic quartzite, schist and gneiss cobbles and boulders up to 1 meter in size (Kelly *et al.,* 2005).

Figure 11. Photograph of the El Rito Formation in the Cañones Fault Zone.

Tal- Lower Abiquiu Formation- The lower member of the Abiquiu Formation is Late Oligocene in age. K-Ar ages on a basalt near its base and $^{40}Ar/^{39}Ar$ ages on the Amalia Tuff in the Upper Abiquiu Formation bracket the age of the Lower Abiquiu Formation between 25.1 and 27, Ma (Smith *et al.*, 2002, Moore, 2000). It is dominated by gray to pinkish conglomerate and sandstone that, based on age and extensional cross-cutting relationships, are interpreted to have deposited in a syn-rift alluvial fan environment (this study). It is poorly sorted, weakly to moderately indurated and calcareous. Conglomerate clasts are typically Proterozoic granites and quartzites that vary in size up to 1 meter. Thickness of this unit varies up to 60 meters (Kempter *et al.*, 2007).

Tr - Ritito Formation- The Ritito Formation was originally included in the Abiquiu formation as the lower member (Tal) (Smith, 1938; Church and Hack, 1939), but based on major differences in lithology and provenance, has since been determined to be a separate formation altogether (Maldonado and Kelley, 2009). It is made up primarily of conglomerate containing subrounded to subangular pebble to cobble-sized clasts in a gray to pinkish sandy matrix. Locally the conglomerate consists primarily of Proterozoic quartzite and granite clasts ranging in size from pebble up to boulder,. The unit is exposed in several localities between the Tusas Mountains and the Nacimiento Mountains. Due to the age of this unit, outcrops located at high structural positions and the fact that it unconformably overlies the syn-Laramide El Rito Formation, the Ritito has been proposed to be related to the earliest stages of rift formation (Vazzana and Ingersoll, 1981). The clast content and paleoflow data are similar to that of the underlying El Rito Formation (Hamilton, 2009). This suggests that the same basins active during late Laramide, that were filling with El Rito sediments, were also the first basins to record syn-rift activity, by filling with Ritito Formation. The fact that the Ritito Formation is preserved at high elevations (see Figure 9 near the Nacimiento Uplift), suggest that these former basins were inverted and not down dropped further during rifting.

Tau- Upper Abiquiu Formation- The upper member of the Abiquiu Formation (Figure 10) consists of beige to white to gray interbedded shales, sandstones, conglomerates and tuffs. It ranges in age from Late Oligocene to Early Miocene. The proportion of volcanic lithic fragments increases toward the top of the formation. In the study area south of the Chama River this unit reaches a maximum thickness of 350 meters (Kempter *et al*., 2007).

Tb- Lobato Formation- The Lobato Formation consists of two separate volcanic members: the Pliocene Lobato Andesite and Lobato Basalt. K-Ar dating has determined an age of 7 Ma for both the basalt and andesite. It is thought to be sourced from many separate volcanic vents and is widely distributed around the northeast margin of the Jemez Mountains (Manley and Mehnert, 1981). The Lobado Basalt ranges in thickness up to 200 meters in some areas (Aldrich and Dethier, 1990). In the local study area however, it is considerably thinner. For the purposes of this study it is confined to the southwestern corner of the mapped area (mapped by Hicks, 2008). It is of particular importance in this study as it is dated at 7 Ma and is offset by the Cañones Fault.

Figure 12. Photograph of Upper Abiquiu Formation in southern portion of the Cañones Fault Zone.

Teb- El Alto Basalt- The El Alto Basalt is not located in the immediate study area , but is relevant to the study because it crosses the Cañones Fault and shows no offset (Gonzalez and Deither, 1991). It is dark brown to black vesicular basalt and contains plagioclase, pyroxene and olivine phyenocrysts. It overlies basaltic andesite of Cañones Mesa and reaches thickness of up to 120 meters (Kelly *et al.*, 2005). K-Ar dating reveals an age of 3 Ma (Manley and Mehnert, 1981).

Qal- For the purposes of this study, all Quaternary units in the mapped area are included under the nomenclature Qal. This unit includes both slightly lithified rocks and loose unconsolidated rocks with extreme variation in clast size ranging from silt to boulder. This unit is primarily confined to stream beds and nearby floodplain. Thicknesses vary up to a maximum of 8 meters (Kempter *et al*., 2007).

2.2 Geologic Mapping

Geologic mapping was carried out in the area along the Cañones Fault zone north of the Chama River and State Highway 84 between the town of Abiquiu, New Mexico and Lake Abiquiu during the 2011 summer field season (Figure 1). The area was mapped at a scale of 1:6000. The mapping area was chosen for its well exposed outcrops that record Laramide shortening and Neogene extension in addition to a well-exposed cross sectional outcrop of the Cañones Fault zone juxtaposing the Jurassic Todilto and Entrada Sandstone in the hanging wall and Permian Cutler Group rocks in the footwall (Figure 2). The 1:6000 map scale was chosen so that details of the relationship between Laramide shortening and Neogene extensional structures could be mapped.

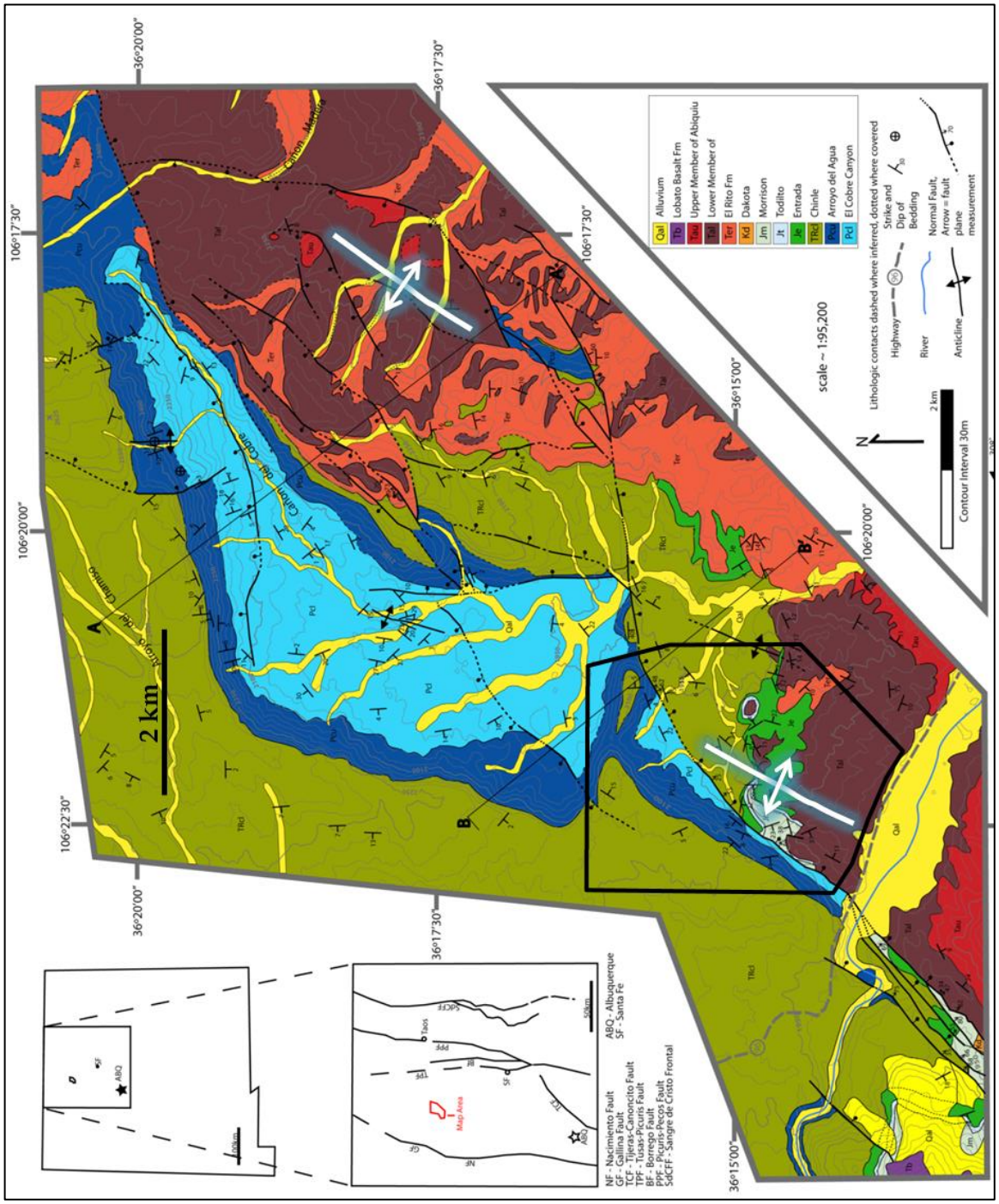

Figure 13. Geologic map of Cañones Fault Zone. Primary study area outlined in black (modified from Hamilton, 2009).

In addition, a larger map was compiled from maps presented in Hamilton (2009), Hicks (2008) and Kempter (2007) at a scale of 1:95000 which encompasses the south-central

and northern portions of the Cañones Fault Zone (Figure 13). It is used expand observations and interpretations to a more regional scale.

2.3 Fault Damage Zone Data Collection

Data collection efforts for the fault damage zone study were focused along the central portion of the Cañones Fault where ephemeral stream cuts expose a large section of rock perpendicular to the fault plane. Fault-damage-zone data were collected from literature where publically available. The outcrop exposed along the Cañones Fault juxtaposes Jurassic Todilto Limestone directly atop Jurassic Entrada Sandstone in the hanging wall and the Permian Upper Cutler Formation in the footwall (Figure 9). The scanline method of data collection was used (Fossen *et al.*, 2007; Berg and Skar, 2005; Faulkner *et al.*, 2010; Mitchell and Faulkner, 2009; Savage and Broadsky, 2010; and others). A five meter long rope, sectioned off per meter with tape, was laid across outcrops of Entrada Ss. and Todilto Ls. (Figure 2) parallel to bedding and perpendicular to the Cañones Fault from the fault core into the hanging wall for reasons stated in section 1.1. Deformation bands were tallied per meter in the Entrada Sandstone and fractures were counted per meter in the Todilto Limestone where rock was accessible. Location of scanline data collection is annotated in red lines in Figure 14 for the fractured Todilto Limestone, and in Figure 15 for the deformation banded Entrada Sandstone.

2.3.1 Fractures

Fracture spacing and density has been shown to decrease with increasing bed thickness (Wu *et al.*, 1995; McQuillan, 1973; Laderia *et al.*, 1973). To avoid inconsistencies in

scanline data collection, fractures used in this study are restricted to those that are confined to the Todilto Limestone Formation and span its thickness. Fracture data collection locations in the Todilto Limestone are annotated on figure 14 along with fracture orientation in stereonet by location.

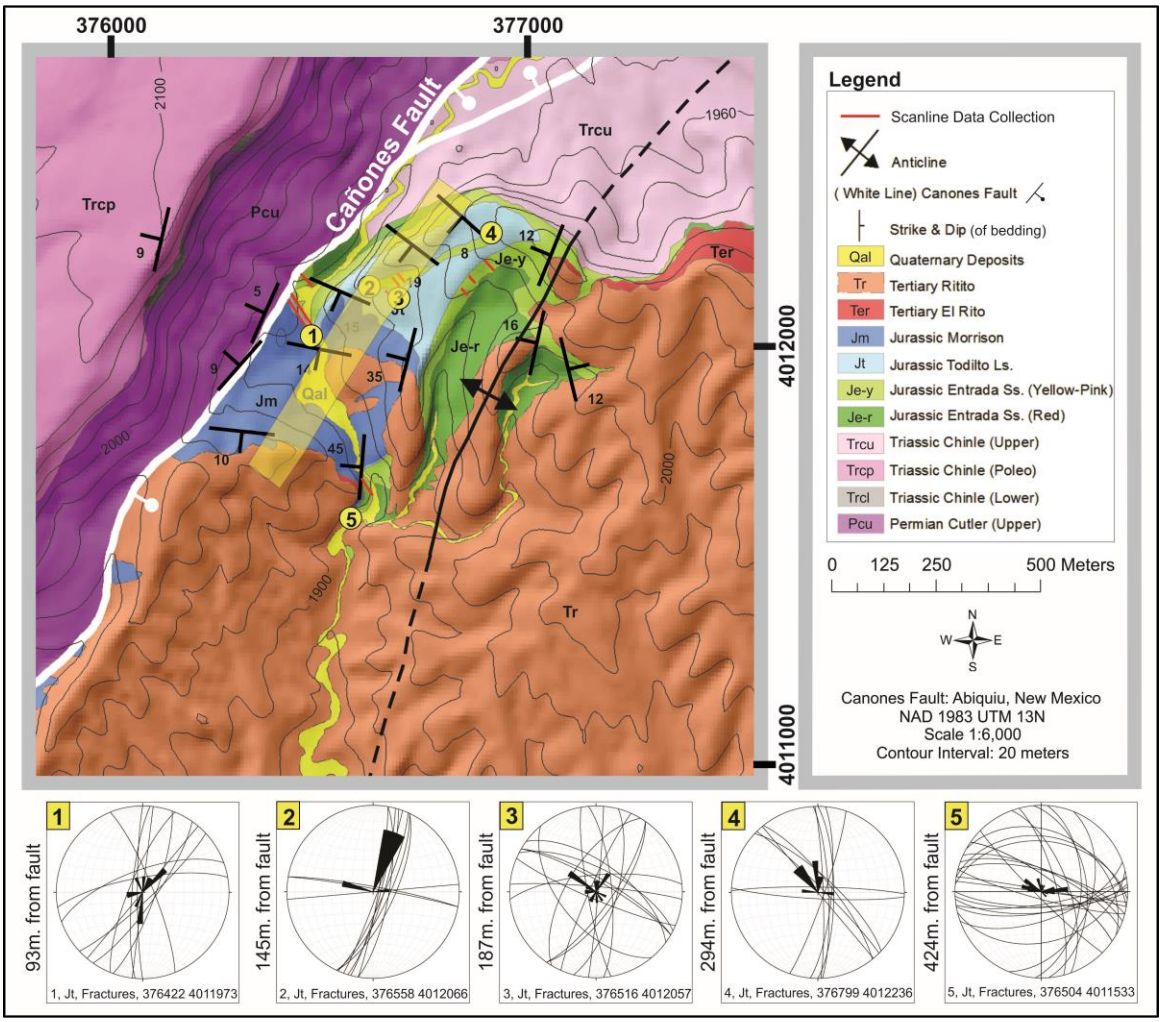

Figure 14. Geologic map showing location of fracture data collection (circled numbers in order of distance from primary fault slip surface), and location of fracture scanline data collection (red lines oriented approximately perpendicular to Cañones Fault and Laramide monocline. Yellow stripe is "structural boundary" that shows range of damage zone margin extents in Todilto Ls. Based on fracture orientation and structural element density distribution from scanline data.

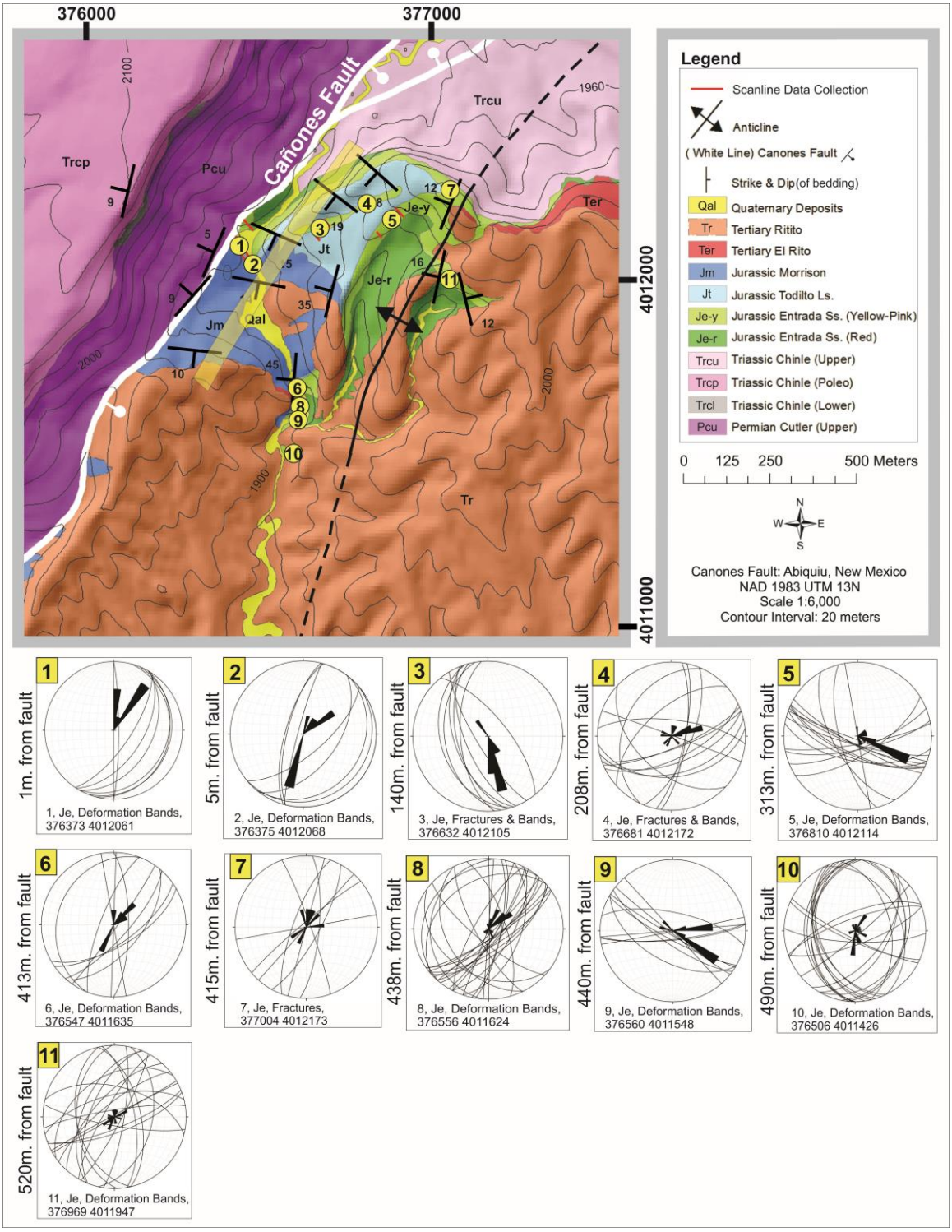
376000
377000
4012000
4011000
Cañones Fault
Trcp
Pcu
Trcu
Ter
Jt
Je-y
Je-r
Jm
Qal
Tr
2100
1960
2000
1900
Legend
Scanline Data Collection
Anticline
(White Line) Canones Fault
Strike & Dip(of bedding)
Qal Quaternary Deposits
Tr Tertiary Ritito
Ter Tertiary El Rito
Jm Jurassic Morrison
Jt Jurassic Todilto Ls.
Je-y Jurassic Entrada Ss. (Yellow-Pink)
Je-r Jurassic Entrada Ss. (Red)
Trcu Triassic Chinle (Upper)
Trcp Triassic Chinle (Poleo)
Trcl Triassic Chinle (Lower)
Pcu Permian Cutler (Upper)
0 125 250 500 Meters
N
W E
S
Canones Fault: Abiquiu, New Mexico
NAD 1983 UTM 13N
Scale 1:6,000
Contour Interval: 20 meters
1m. from fault
1, Je, Deformation Bands, 376373 4012061
5m. from fault
2, Je, Deformation Bands, 376375 4012068
140m. from fault
3, Je, Fractures & Bands, 376632 4012105
208m. from fault
4, Je, Fractures & Bands, 376681 4012172
313m. from fault
5, Je, Deformation Bands, 376810 4012114
413m. from fault
6, Je, Deformation Bands, 376547 4011635
415m. from fault
7, Je, Fractures, 377004 4012173
438m. from fault
8, Je, Deformation Bands, 376556 4011624
440m. from fault
9, Je, Deformation Bands, 376560 4011548
490m. from fault
10, Je, Deformation Bands, 376506 4011426
520m. from fault
11, Je, Deformation Bands, 376969 4011947

Figure 15. Geologic map showing location of deformation band data collection (circled numbers in order of distance from primary fault slip surface), and location of deformation band scanline data collection (red lines oriented approximately perpendicular to Cañones Fault and Laramide monocline. Yellow stripe is "structural boundary" showing range of extent for outer damage zone margin in Entrada Ss. based on deformation band orientation and structural element density distribution from scanline data.

2.3.2 Deformation Bands

Deformation band data collection was confined to the upper most yellow colored section of the Entrada Sandstone to avoid any inconsistencies that may arise due to the possibility of differing mechanical properties between the three colored layers present in the Entrada Sandstone in the study area (yellow – top, pinkish white – middle, red – base). This is because deformation bands were observed to be less dense in the lower two portions of the Entrada Ss. relative to the upper yellow portion. No distinction was made between deformation bands formed as a single structure and those formed in aggregate clusters. Deformation band data collection locations in the Entrada Sandstone are annotated on Figure 15 along with deformation band orientation in stereonet by location.

2.3.3 Data Plots

Data plots include my data and that presented in previously published papers. This compilation was conducted by the author and the Shell Exploration and Production Research Team. All data is plotted on linear-linear scales with the exception of the "Fault throw vs. Damage Zone Width" data which are plotted using a log-log scale.

3. CANONES FAULT AND MONOCLINE KINEMATICS

The Cañones Fault Zone extends across the field area with an overall northeast trending strike. Along the central portion of the fault, throw is concentrated along a single trace. The fault splays into a series of predominantly northeast striking branches both south of the Chama River and in the northern portion. Between the north and central portions of the Cañones Fault lies a zone of nearly east-west striking faults (Figure 13). This zone of east-west trending structures marks a change in dip polarity from primarily southeast dipping structures to the south along the southern and central portions of the Cañones Fault Zone to northwest-dipping structures in the northern portion. This zone of east-west striking faults is therefore interpreted to transfer strain between the northern and central portions of the Cañones Fault. Both north and south of the east-west trending transfer zone, a monocline is present in the hanging wall of the extensional faults. To the south the monocline is east-vergent and to the north it is west vergent (Figure 13).

3.1 Mapping

In the primary field area 1:6000 scale mapping was concentrated along the central portion of the Cañones Fault Zone (Figure 1). In this area the Cañones Fault is steeply dipping (68˚SE) to the southeast and trends northeast. In the northern portion of this area the Cañones Fault consists of several splays and change strike to nearly east-west. In the mapped area, the central portion (as defined above) of the Cañones Fault is located in the forelimb of a Laramide aged shortening related monocline (Figure 1). It was also considered that the monocline may have formed in the Cañones Fault hanging wall as part of a roll-over anticline. This is shown to not be the case based on the following

unconformity and cross-cutting relationships. Folded Jurassic age rocks from the Morrison Formation, Todilto Limestone and Entrada Sandstone are eroded and unconformably overlain by the Cenozoic Ritito Formation (Figure 16). The Ritito Formation is then cut by the Neogene Rio Grande Rift related Cañones Fault. This cross-cutting relationship is evident by the presence of the Ritito Formation in the hanging wall of the Cañones Fault and its presence near the top of Cerro Pedernal located approximately 4 miles to the south at an elevation of 9000 ft. (approximately 2500 ft. higher elevation than the study area) on the footwall side of the fault.

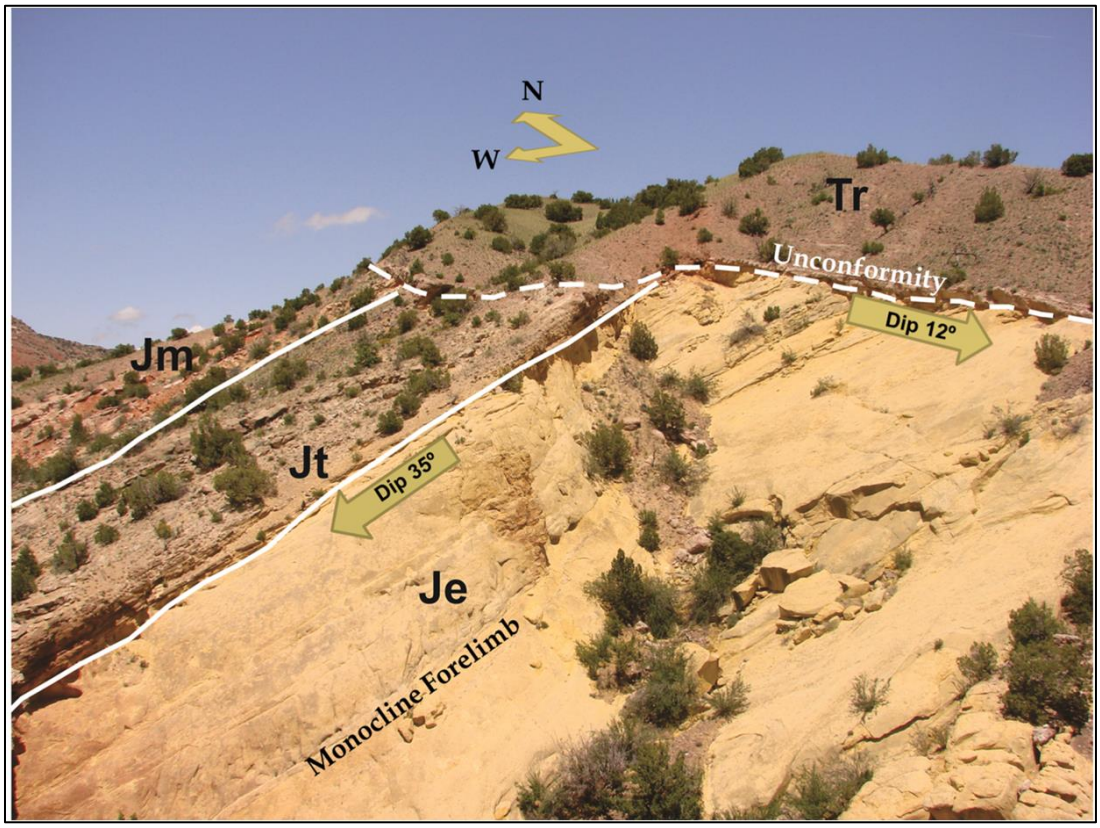

Figure 16. Field photograph showing angular unconformity between Tertiary Ritito (Tr) Formation and underlying tilted Jurassic Entrada (Je), Todilto (Jt) and Morrison (Jm) formations in the forelimb of Laramide monocline. (unconformity dip 12°SE, monocline forelimb dip 35°NW)

3.2 Cross Section construction and restoration

Cross section construction and restoration were carried out at three locations along the trace of the central to northern portions of the Cañones Fault Zone, perpendicular to the fault and monocline (Figure 1). Sections were constructed and restored by hand. The southernmost section A-A′ (Figure 17) shows the Cenozoic angular unconformity between the Ritito and the Jurassic age rocks (Figure 16). 450 meters of throw and 175 meters of heave have been interpreted across the Cañones Fault at this location. By line length restoration, 170 meters of extension and 76 meters of shortening have been interpreted across the Cañones Fault and

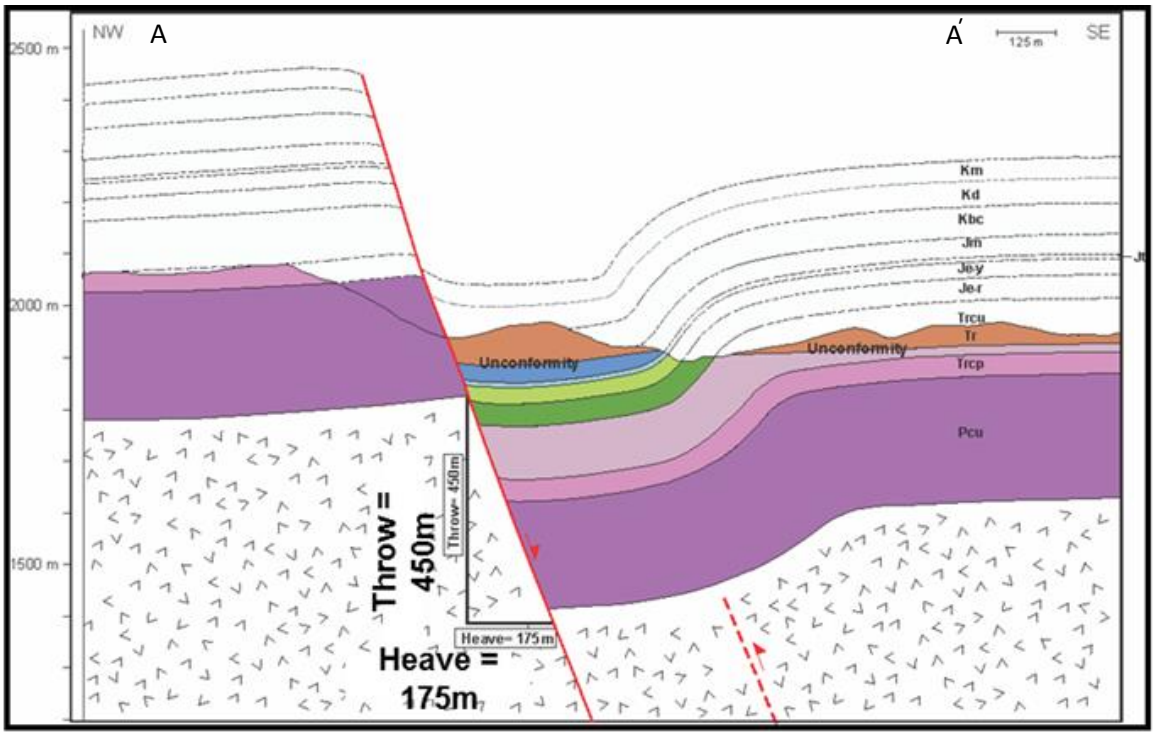
NW
A
A′
SE
125 m
2500 m
2000 m
1500 m
Km
Kd
Kbc
Jm
Je-y
Je-r
Trcu
Tr
Trcp
Pcu
Unconformity
Unconformity
Throw = 450m
Throw= 450m
Heave= 175m
Heave = 175m

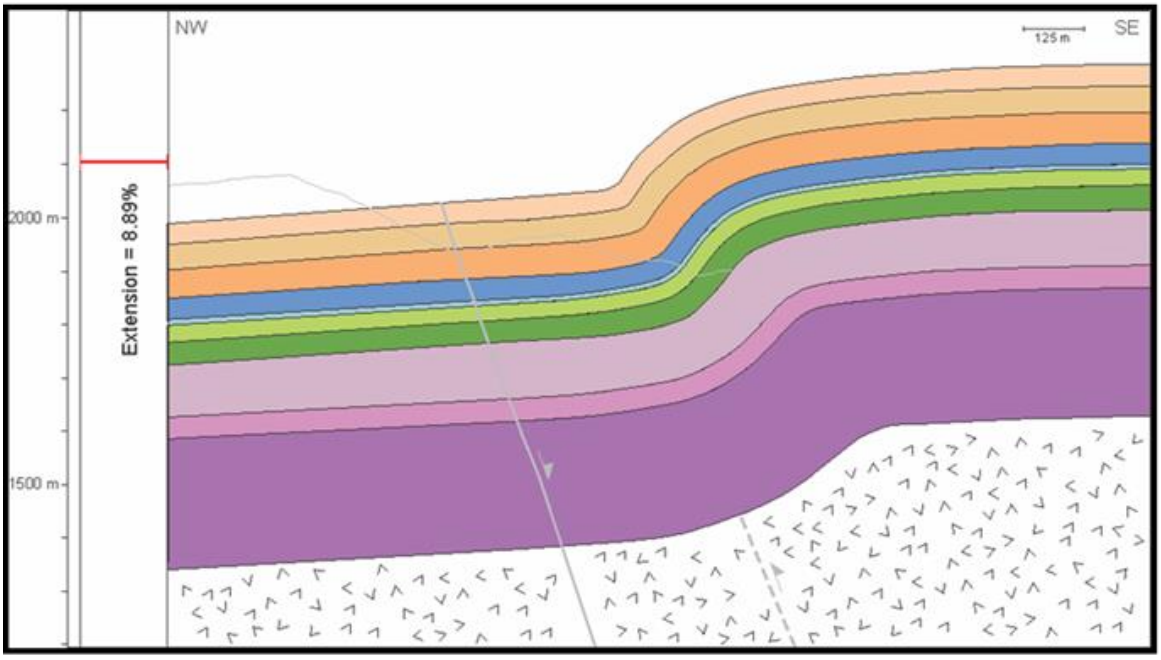
NW
SE
125 m
2000 m
1500 m
Extension = 8.89%

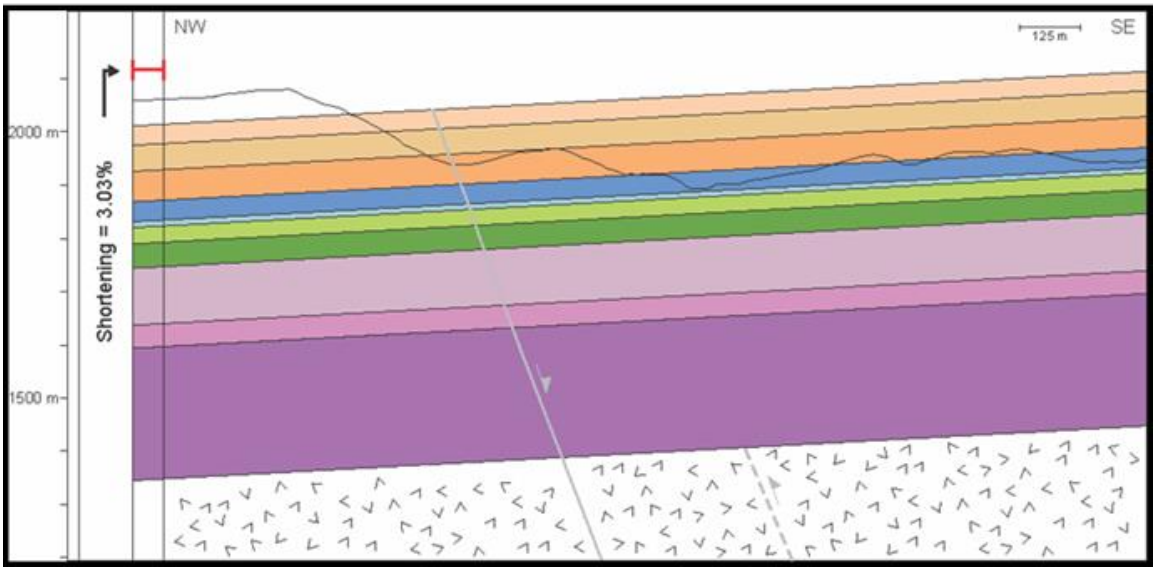

Figure 17. Cross section A-A' (Figure 1) and restored extension and restored shortening across the Cañones Fault and Laramide monocline. 170 meters extension and 76 meters of shortening.

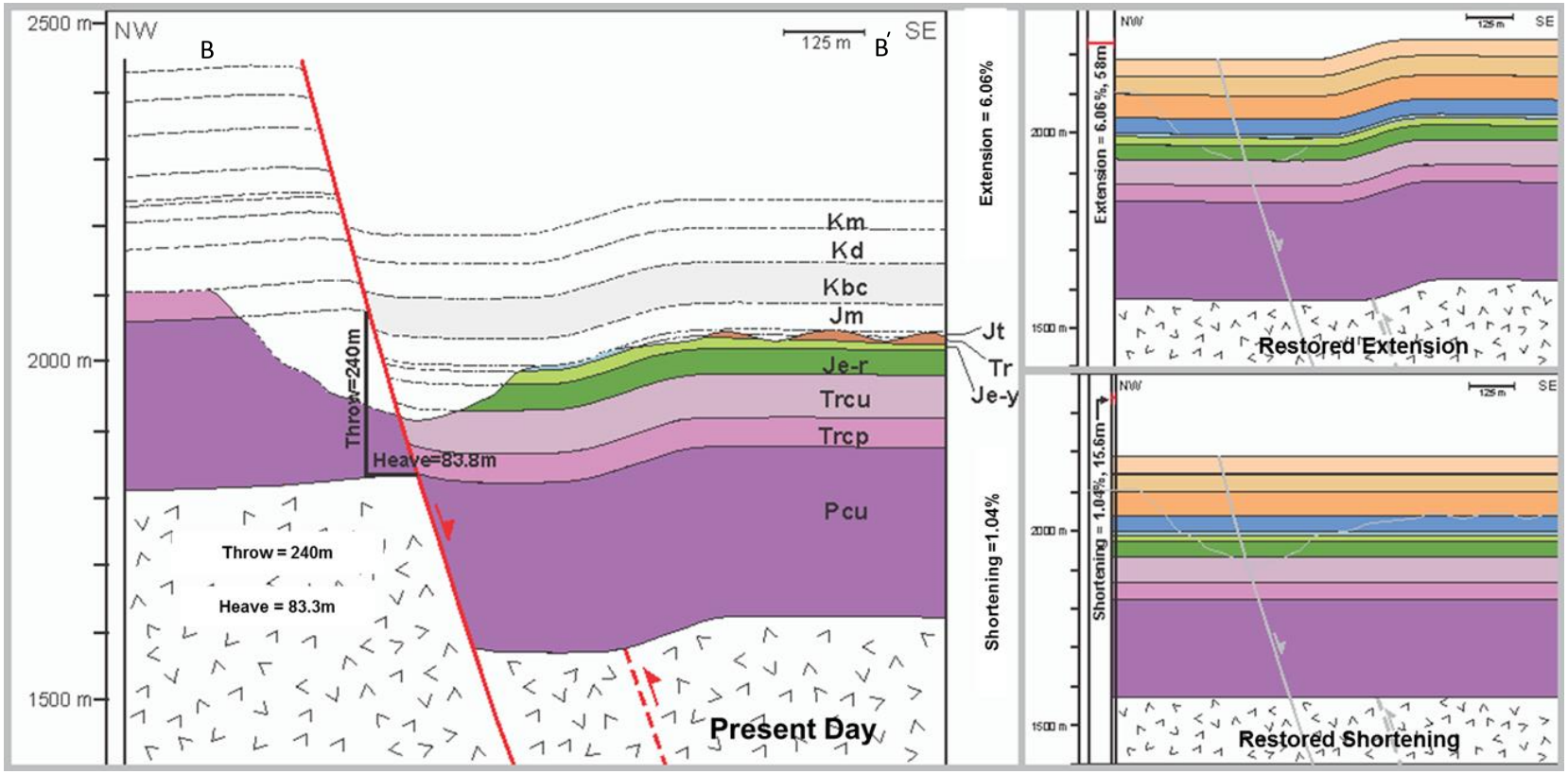

Figure 18. Cross section B-B' (Figure 1) and restored extension and restored shortening across the Cañones Fault and Laramide monocline. 58 meters of extension and 16 meters of shortening.

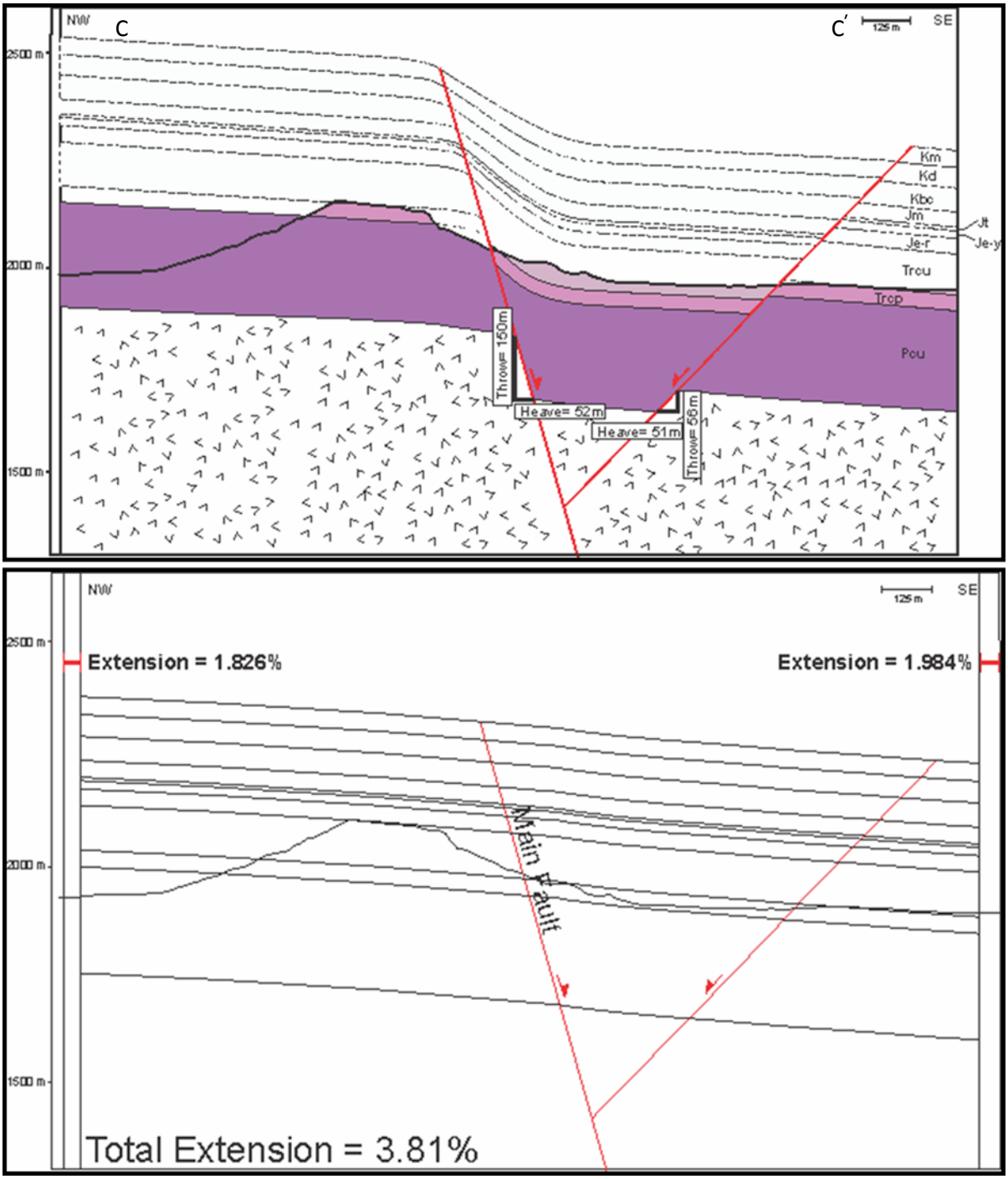

Figure 19. Cross section C-C' (Figure 1) and restored extension across the Cañones Fault. 42 meters overall extension.

Laramide age monocline respectively. In the cross section B-B′ taken (Figure 18) to the north of A-A′, a decrease in throw to 240 meters and a heave of 83 meters is interpreted. Restored extension across the Cañones Fault shows 58 meters and shortening related to the monocline has decreased from south to north to 16 meters. The northernmost cross section C-C′ (Figure 19) taken perpendicular to the Cañones Fault Zone shows the main trace of the Cañones Fault and a more shallowly dipping (~55˚NW) branched antithetic fault splay. Throw on the Cañones Fault is 150 meters with a heave of 52 meters and throw on the branched antithetic is 56 meters with a heave of 51 meters. Shortening related to the monocline terminates and the fault trace trends more east-west. At this location on the fault extension has decreased to 42 meters overall, ~2% on the main trace of the Cañones Fault and ~2% extension from the shallow branched antithetic fault.

From south to north along the Cañones Fault throw decreases from 450 meters to 150 meters. Extension across the Cañones Fault and shortening related monocline also decrease from south to north almost linearly (Figure 20).

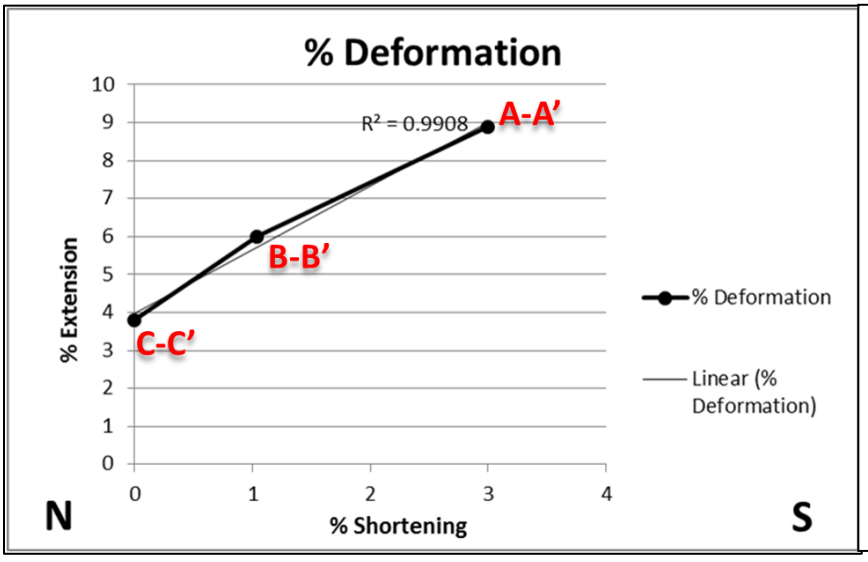

Figure 20. Percent extension versus present shortening across three restored cross sections across the Cañones Fault and Laramide monocline.

4. FAULT DAMAGE ZONE RELATIONSHIPS

A fault damage zone is an apron of damage including fractures, joints and/or deformation bands depending on lithology and subsidiary slip surfaces; all enveloping a primary fault slip surface. For the purposes of this study fault damage zones are divided into two end member types on the basis of lithology and primary structural element hosted by the protolith rock. These are fractured fault damage zones and deformation banded fault damage zones. This distinction is important because fractures provide conduit to flow in subsurface aquifers and petroleum reservoirs and deformation bands are known to act as baffles to fluid flow. Fractured fault damage zones occur primarily in more brittle less granular lithologies such as limestone and other carbonates, mudrock and crystalline rocks (Billie *et al.,* 2003; Micarelli *et al.,* 2006; Savage and Brodsky, 2010; Mitchell and Faulkner, 2009; Faulkner *et al.,* 2010 respectively). Deformation banded fault damage zones occur in porous granular lithologies such as eolian and fluvial sandstone and carbonate grainstone (Fossen *et al.,* 2007; Berg and Skar, 2005; Schueller *et al.,* 2013; Tondi *et al.,* 2005; and others).

4.1 Structural Element Density Distribution

Structural element density distribution-the distribution of fractures and deformation bands within the confines of the fault damage zone is shown to vary by lithology. However in both types of damage zones, fractures and deformation bands are observed to have the highest concentration near the fault core and decrease to background levels at varying rates toward the margin of the fault damage zone. This is consistent with observations made in other studies (Fossen *et al.,* 2007; Du Bernard *et al.,* 2002; Mitchell

and Faulkner, 2009; Faulkner *et al.*, 2010; Savage and Broadsky, 2010; and others). The exact distance from the fault core, at which background levels are reached is subjective and varies by data availability, study method, and author preference. Methods of background definition varying by author and study are as follows: Some workers define background damage as the fracture density of damage that can be measured by scanline in a relatively unfaulted/undeformed area of host rock (Mitchell and Faulkner, 2009; Faulkner *et al.*, 2010; and others). Others choose an outer damage zone margin where along a scanline, there are several consecutive meters devoid of deformation bands (Schueller *et al.*, 2013). Berg and Skar (2005) define the deformation banded fault damage zone outer margin where a structural density curve depicting deformation density per meter from the fault core shifts from a curved or semi linear slope with a high gradient to a more linear slope with a low gradient. Other workers define background as the point along a measured scanline where fractures and/or deformation band counts per meter reach repeated counts per meter at low levels relative to densities more near the fault core. The latter approach was used in this study, because unlike previous methods mentioned, this study is aimed at understanding lithological effects on density distribution of structural elements in the two end member type fault damage zones, and therefore treat the Jurassic Todilto Limestone and Jurassic Entrada Sandstone in a holistic manner.

4.1.1 Deformation Banded Fault Damage Zones

Fault damage zones in porous granular material exhibit a character of strain distribution where deformation bands and subsidiary slip surfaces form in high density clusters

adjacent to the primary fault slip surface and decay exponentially to back ground levels into the hanging wall (Fossen *et al.*, 2007 and this study). At the Cañones Fault (throw 450 meters), deformation band density measurements in eolian Entrada Sandstone (this study) (Figure 21) are highest near the fault core, and decay, fit to a power law regression, to background deformation levels. Similar fits to power law regression are shown in data presented in Fossen *et al.* (2007) where deformation

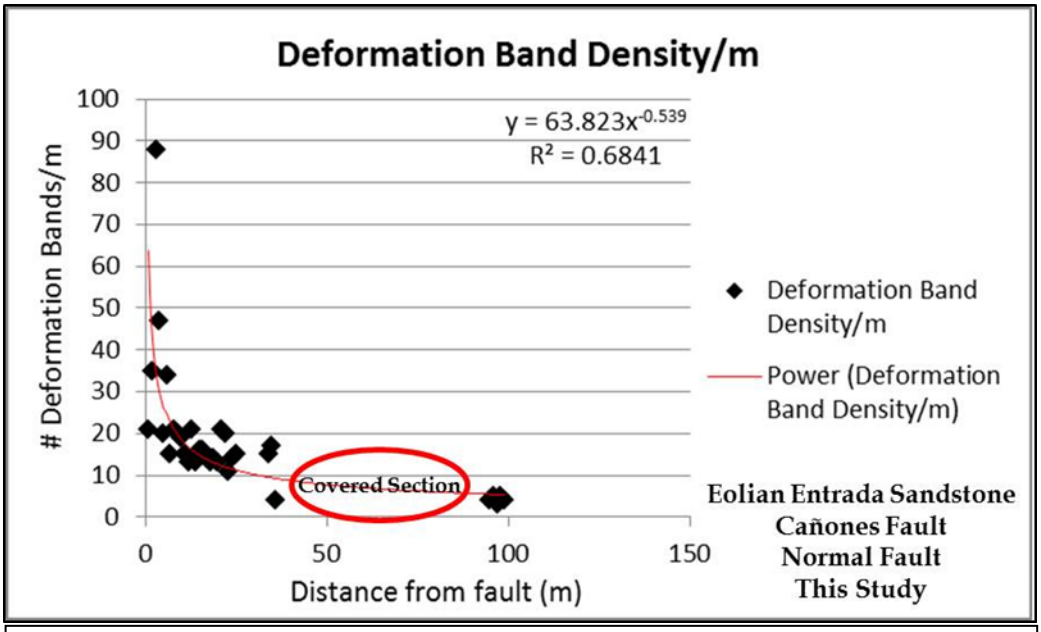

Figure 21. Deformation band density from fault core (zero on the x-axis), into the hanging wall damage zone of the Cañones Fault. Jurassic Entrada Sandstone (data from this study, New Mexico).

band densities were measured in interbedded fluvial sandstone (Figure 22 a and b) and eolian sandstone (Figure 23 a and b) in the hanging wall of a 15 meter throw fault. The overall power law-decrease of deformation band density with increasing distance from the fault core observed in both studies is interpreted to be scale invariant. This is due to similar power law regression fits to deformation band density data collected at faults of

differing throw (Cañones Fault, 450 meters throw and Fossen *et al.* (2007), 15 meters throw).

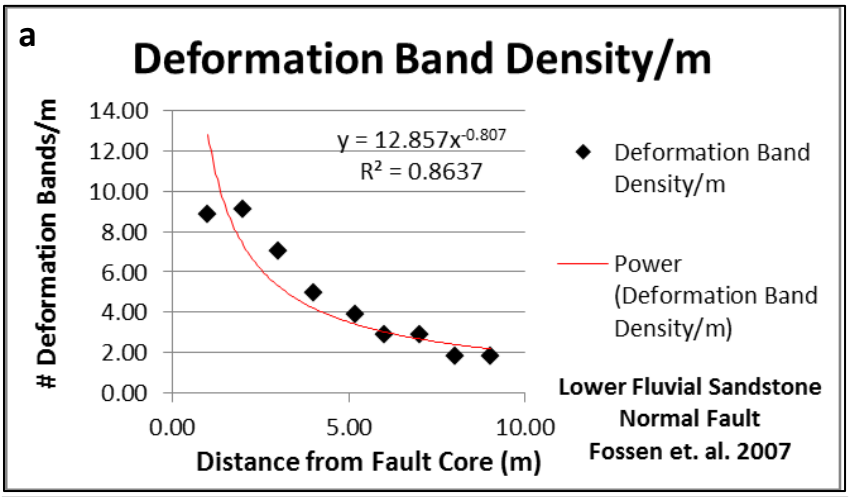

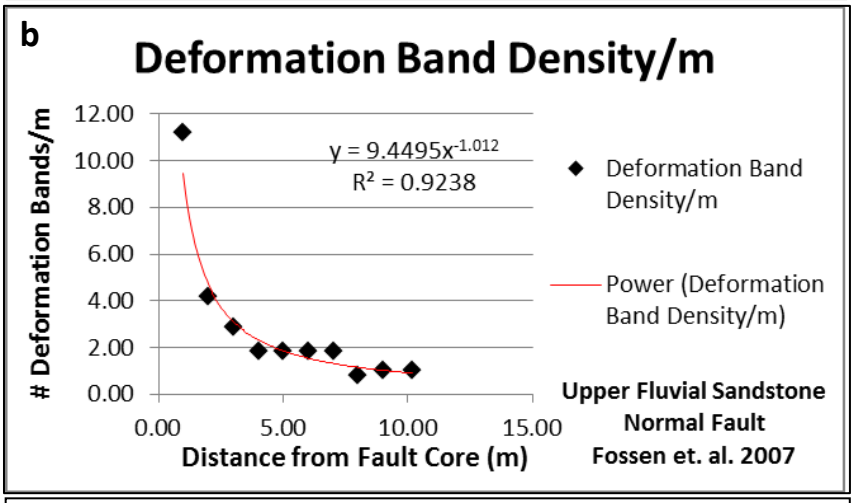

Figure 22 a and b. Deformation band density from fault core, (zero on x-axis) into the hanging wall fault damage zone in fluvial sandstone. Fault throw 15 meters (data modified from Fossen et.

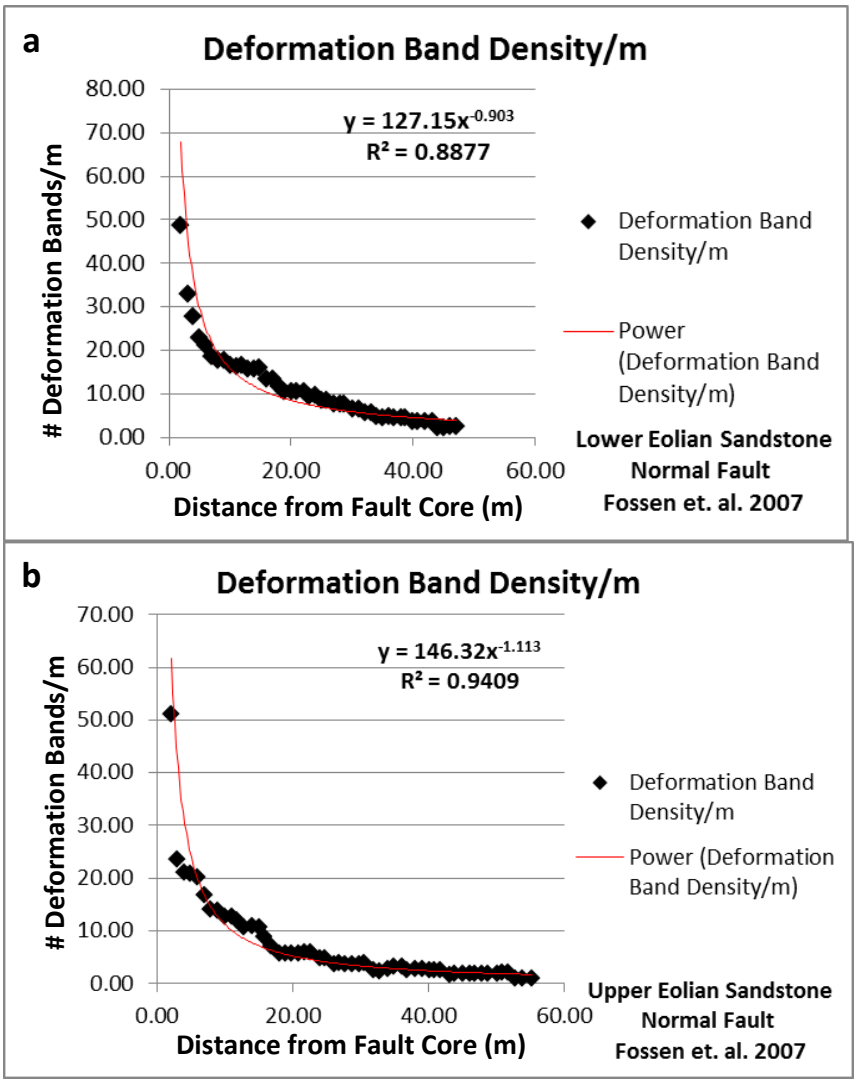

Figure 23 a and b. Deformation band density from fault core, (zero on x-axis) into the hanging wall fault damage zone in Eolian sandstone. Fault throw 15 meters (data modified from Fossen et.

4.1.2 Fractured Fault Damage Zones

Unlike data collected in deformation banded fault damage zones, fracture density data collected in brittle fault damage zones typically does not fit a power law regression.

Fractured fault damage zones typically formed in brittle, non-granular rocks exhibit a character of strain

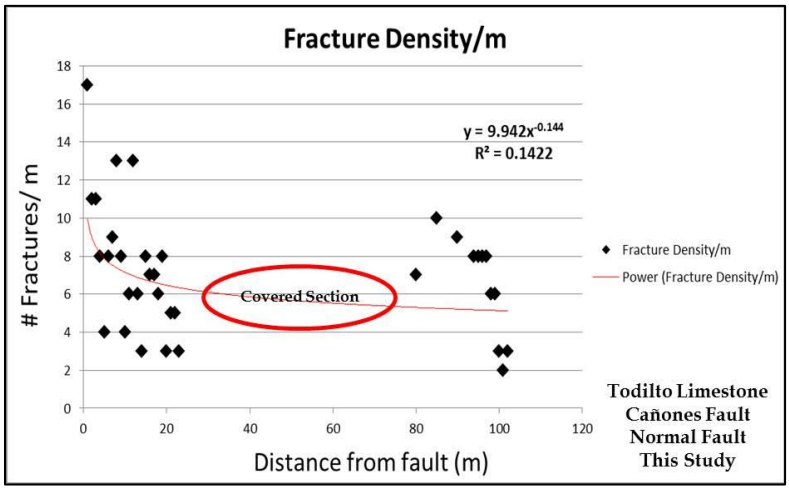

Figure 24. Fracture density from fault core (zero on the x-axis), into the hanging wall damage zone of the Cañones Fault. Jurassic Todilto Limestone. Throw 450 meters (data

distribution where fracture density is highest adjacent to the fault core, and ranges from zero fractures per meter to levels observed adjacent to the primary fault slip surface throughout the hanging wall. At the Cañones Fault (throw 450 meters) damage zone, fracture density data collected in the brittle Todilto Limestone exhibit this character (Figure 24). Similar fracture distributions were observed at large offset strike-slip faults formed in igneous rock by Faulkner *et al.* 2010 and Mitchell and Faukner (2009) (Figure 25 a-c). Eichhubl and Boles (1998) observed similar fracture density distribution in extensional faults formed in porcelanite and dolomite (Figure 26 a and b).

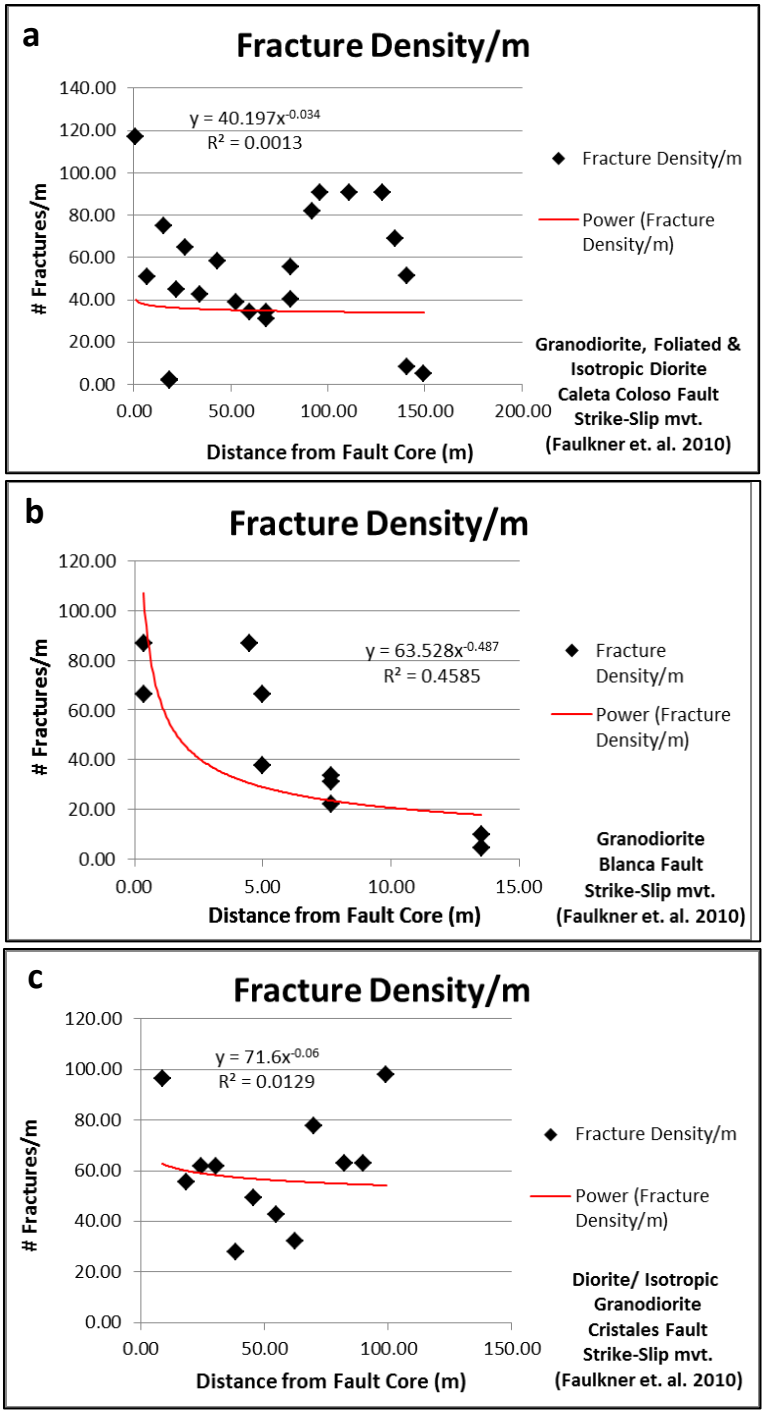

Figure 25 a, b and c. Fracture density from fault core (zero on x-axis) into wall rock damage zone of strike-slip faults in crystalline rock. Fault throw a) 5000 meters, b) 200 meters, c) 35 meters (data modified from Faulkner et. al. 2010).

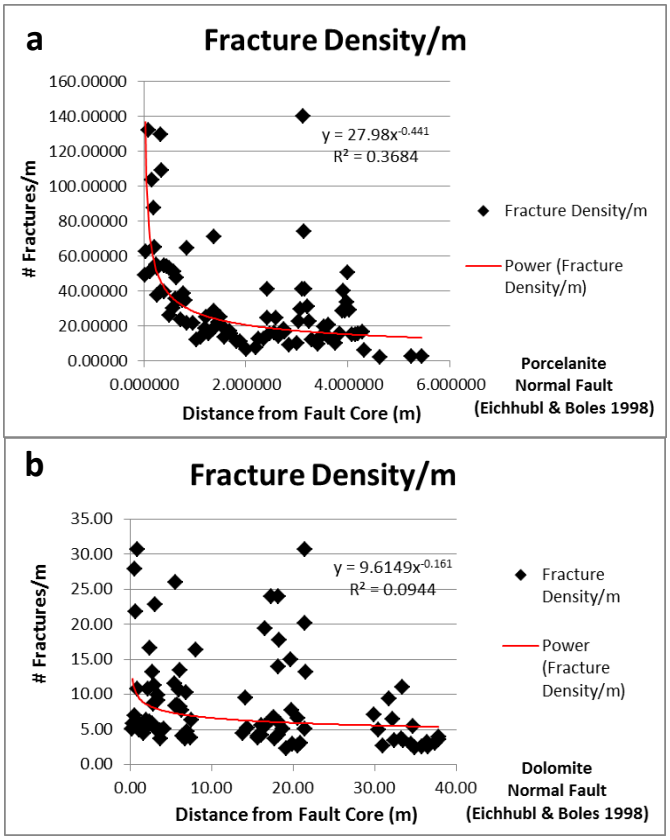

Figure 26 a and b. Fracture density from fault core (zero on x-axis) into hanging wall damage zone in a) dolomite and b) porcelanite. Fault throw unknown

Savage and Broadsky (2010) observed fracture density distribution in the hanging wall damage zone of three relatively low offset extensional faults (0.3-1.2 meters) in soft siliceous mudstone to be more like that observed in porous granular rocks where deformation bands are the dominant manifestation of strain. High densities of fracturing were observed to be clustered near the fault core and decay exponentially toward the damage zone margin and fit to a power law regression (Figure 27). This contrast between the distribution of damage zone fractures observed in Savage and Broadsky (2010) and

those observed in this study, Eichhubl and Boles (1998), Mitchell and Faulkner (2009) and Faulkner *et al.* (2010) are likely due to lack of brittleness of the deformation hosting soft silicious mudstone in Savage and Broadsky (2010). Marshall and

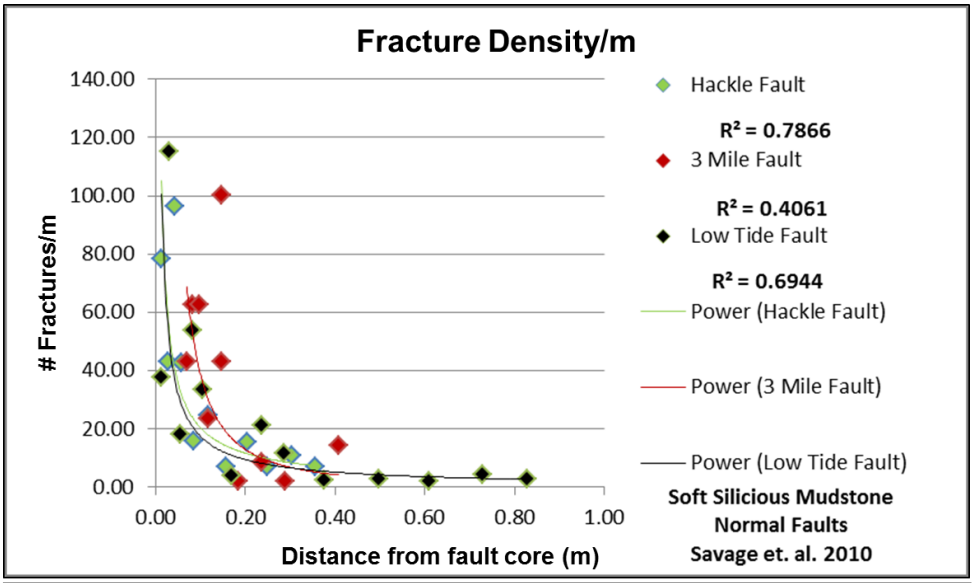

Figure 27 a and b. Fracture density from fault core (zero on x-axis) into hanging wall damage zone in siliceous mudstone of the Monterey Formation in California. Fault throw Hackle Fault 0.53 meters, 3 Mile Fault 1.2 meters and Low Tide Fault 0.35 meters (data modified from Savage et. al. 2010).

Faulkner (2009) documented exponential decreases in micro-fracture density distribution in thin section from the fault core into wall rock of several strike-slip faults in crystalline lithology (Figure 28 a-f). This difference between micro- and macro-fracture damage zone density distributions implies that fault damage zone fracturing in brittle crystalline rock is dependent upon the scale at which data is collected. There is not enough data to suggest the relationship between micro fractures and macro-fractures presented by Mitchell and Faulkner (2009) is present in other fault damage zones.

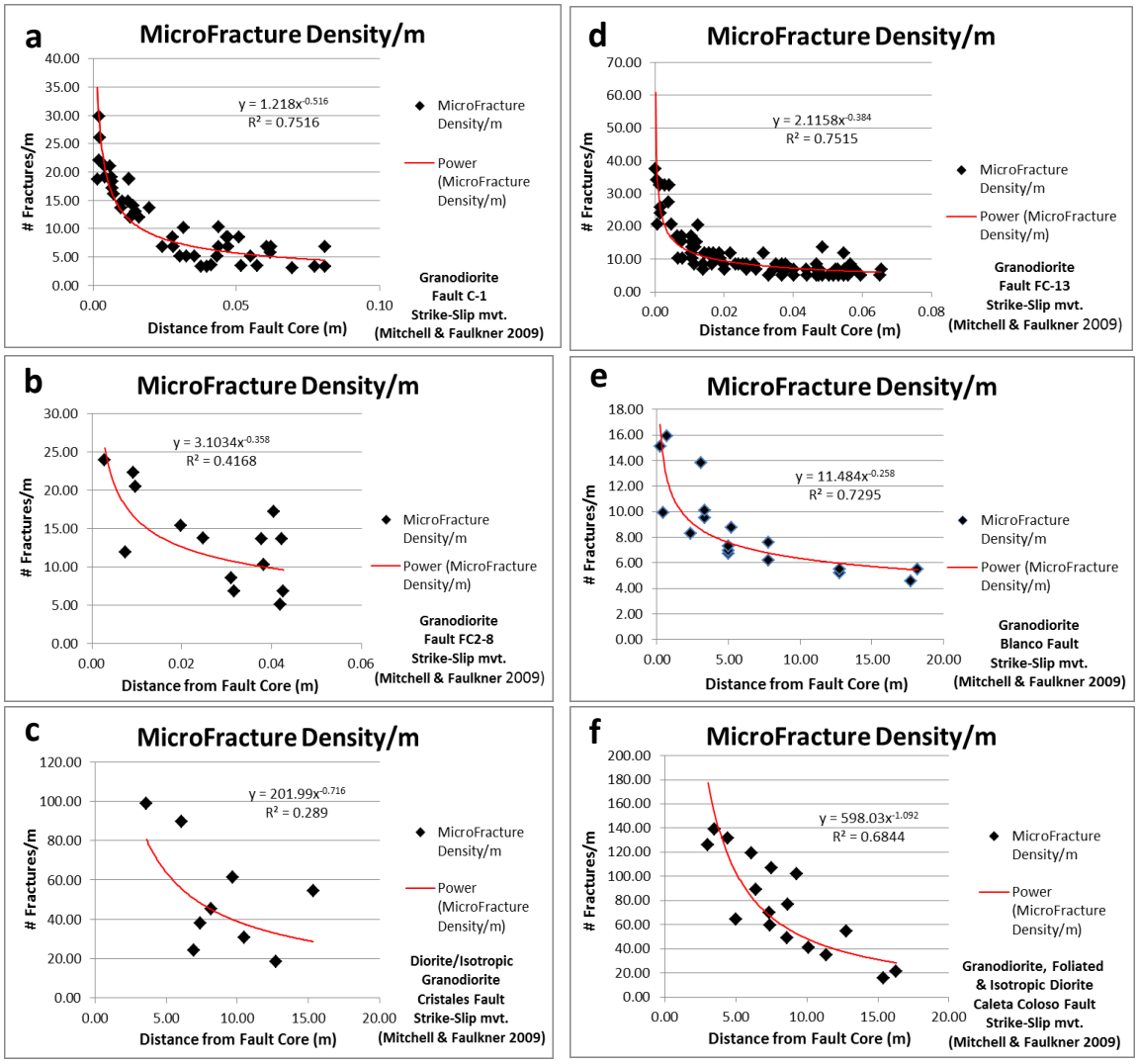

Figure 28 a, b, c, d, e & f. Micro -fracture density from the fault core (zero on the x-axis) into the wall rock of strike-slip faults in crystalline rock. Fault throw a) unknown, b) unknown, c) 200 meters, d) unknown, e) 35 meters, f) 5000 meters (data modified from Mitchell & Faulkner 2009).

4.2 Fault Throw vs. Fault Damage Zone Width

Increasing fault damage zone width (i.e. the width of the damage zone measured perpendicular to the fault surface, from the fault core into the hanging wall or footwall until background damage density levels are met), has been shown to scale with fault throw accumulation in both fractured (Micarelli *et al.*, 2006; Mitchell and Faulkner,

2009; Faulkner *et al.*, 2010) and deformation banded (Du Bernard *et al.*, 2002; Fossen *et al.*, 2007; Knott, 1996; and others) end member type fault damage zones (Figures 29 and 30). Like structural element density distribution within fault damage zones (section 4.1), scaling relationships between fault throw and fault damage zone width can be dependent on the method of background damage definition.

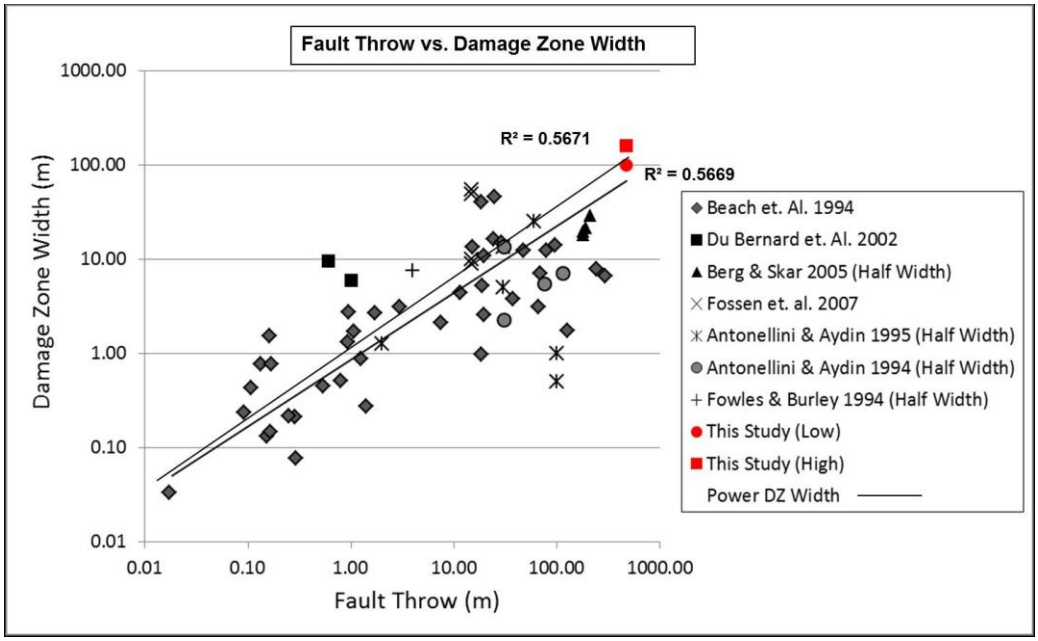

Figure 29. Deformation banded fault damage zone half width. Scaling relationship between fault throw and fault damage zone width from literature and this study (red points). Red square is distal edge (relative to Cañones Fault) of yellow stripe Deformation Band Map, and red circle is proximal edge of yellow stripe on Deformation Band Map.

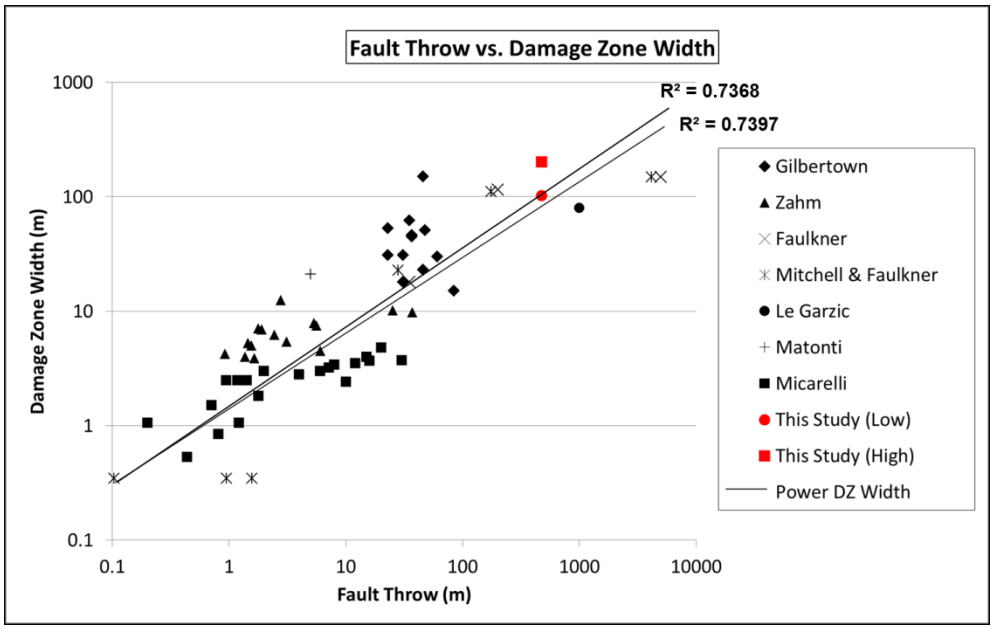

Figure 30. Fractured fault damage zone half width. Scaling relationship between fault throw and fault damage zone width from literature and this study (red points). Red square is distal edge (relative to Cañones Fault) of yellow stripe Deformation Band Map, and red circle is proximal edge of yellow

4.2.1 Deformation Banded Fault Damage Zones

Fault damage zone margins in the deformation banded Entrada Sandstone are defined by a subtle change in orientation of deformation bands from Cañones Fault parallel to a random distribution of orientations associated with the monocline deformation (Figure 15). A structural boundary (yellow stripe) on Figure 15 indicates the range of extents for the fault damage zone margin based on changes in deformation band orientation. In addition to this subtle change in deformation band orientation, background deformation band density, reached at 97 meters into the hanging wall, perpendicular from the fault core is within the range of extent defined by the structural boundary (yellow stripe) in Figure 15. Fault throw vs. width data points collected from the Cañones Fault in the

Entrada Sandstone are consistent with trends observed in data from other fault throw vs. damage zone width data in deformation banded lithologies (Figure 29). Both deformation band density measurements and structural boundary defined by deformation band orientations imply that the outer margin of the Cañones Fault hanging wall damage zone in the Entrada Sandstone is located in the syncline portion of the shortening related monocline forelimb.

4.2.2 Fractured Fault Damage Zones

Like the deformation banded damage zone of the underlying Entrada Sandstone, the fault damage zone margin in the fractured Todilto Limestone is defined by a subtle change in orientation of fractures from Cañones Fault-parallel to a random distribution of orientations associated with the shortening related monocline. A structural boundary (yellow stripe) on Figure 14 shows the range of extents for the fractured fault damage zone margin in the Todilto Limestone based on changes in fracture orientation. In addition to this subtle change in fracture orientation, background fracture density was reached at 99 meters into the hanging wall perpendicular from the fault core, and is within the structural boundary shown on Figure 14. Fault throw vs. width data points collected from the Cañones Fault in the Todilto Limestone are consistent with trends observed in data from other fault throw vs. damage zone width data in fractured lithologies (Figure 30). Both fracture density measurements and structural boundary defined by deformation band orientations imply that the outer margin of the Cañones Fault hanging wall damage zone in the Todilto Limestone is located in the syncline portion of the shortening related monocline forelimb.

5. CONCLUSIONS

Structural reconstructions show that the central portion of the Cañones Fault occurs in the forelimb of a Laramide age monocline. Interpretation of the geologic map shows that beyond termination of the monocline to the north, the Cañones fault changes trend from N40˚E to nearly east-west (Figure 1), and still further north the trace of the Cañones Fault trends approximately N40˚E again as it is located in the forelimb of another Laramide age monocline (Figure 13). The transition between the two Laramide-aged monoclines, where the Cañones Fault trends nearly east-west marks a change in dip polarity of both extensional and shortening related structures from primarily east-dipping faults south of the transition zone to primarily west-dipping faults north of the transition zone. Furthermore, a strong correlation exists between percent of extension and shortening across restored cross sections (Figure 20). These relationships and similarities suggest that pre-existing structures formed due to Laramide shortening have a significant influence on the development and geometry of structures formed under Rio Grande Rift extensional conditions.

There are significant differences in plotted structural-element density distributions between the two end-member type fault damage zones (fractured and deformation banded). As the data are collected from different faults under differing states of stress, distinction cannot be made as to whether the density distribution characteristic of fractured fault damage zones differs from that of deformation banded fault damage zones based on lithologic controls. Fault planes are inherently rough surfaces that often exhibit bends, asperities, and differences in slip rates that will affect the movement and geometry of the hanging wall and thus the distribution of damage zone structures within. In

addition, burial and uplift history experienced by these different faults is not identical. Rocks in the different fault damage zones were therefore subjected to different fluid interactions, affected by different overburden pressures and contrasting changes in principal stresses throughout their formation. Along the Cañones Fault the two end-member type damage zones overlie each other, the Jurassic Entrada Sandstone beneath the Jurassic Todilto Limestone, in the hanging wall (Figure 2). Therefore the two end-member type damage zones have been subjected to identical burial histories and fault plane changes, such that they can be studied together in the context of the effects of lithology on the distribution of damage zone structures and extent of damage from the fault core into the hanging wall (damage zone width).

Figures 21 and 24 show the distribution of deformation bands in the Entrada Sandstone and the distribution of fractures in the Todilto Limestone respectively (this study), in the hanging wall damage zone of the Cañones Fault. Covered section is marked on the plots where inaccessible for scanline measurements. These two plots exhibiting scanline data from this study show striking similarity to those plots of data collected from literature on end-member type fault damage zones, (fractured Figures 25 a-c and 26 a and b) and deformation banded (Figures 22 a and b and 4 a and b). This similarity between damage zones at different faults, divided by the damage zone end-member scheme, suggests that the difference in the distribution of structures within the respective end-member fault damage zones is indeed controlled by the brittleness of the deformation hosting lithology and likely not entirely, but predominantly independent of external factors effecting the fault zone such as burial history and fault plane changes. Further evidence of this supposition is described in Savage *et al.* (2010) where data plotted for three fractured

fault damage zones in soft siliceous mudrock (Figure 27), exhibit similar character to fault damage zones in other softer deformation banded lithologies (Figures 22 a and b and 23 a and b). Empirically derived evidence from Palchik (1999 and 2006) indicates that with increasing host rock granular porosity, strength decreases and the rock therefore becomes less sensitive to confining pressures. These findings are similar to findings in this study where by damage zones in more porous, less brittle rock exhibit a concentration of fractures (Savage *et al.*, 2010) or deformation bands (Fossen *et al.*, 2007; this study) near the fault core that decay exponentially to the damage zone margins.

The relationship between fault throw and fault damage zone width is well defined in Figures 29 and 30 for the two end-member type damage zones. The effect of lithology on fault damage zone width is shown to be negligible in this study. Fracture and deformation band densities in the Todilto Limestone and Entrada Sandstone respectively, decreases with distance from the primary fault slip surface of the Cañones Fault to background levels at the outer margin of the fault damage zone. While the density of damage zone structures is distributed differently among the two end-member type damage zones at the Cañones Fault. The edge at which background levels of damage zone structures are reached (97 meters in the Entrada Sandstone and 99 meters in the Todilto Limestone), and the similarity between the zones of tolerance denoted by the yellow stripes on Figures 14 and 15, derived from the subtle difference in fracture and deformation band orientation from parallel with the Cañones Fault to more parallel with the Laramide age monocline suggest that lithology is not a controlling factor in fault damage zone extent from the primary fault slip surface. As shown by other workers (Fossen, 2000; Beach *et al*., 1994; Berg and Skar, 2005; Fossen *et al.*, 2007; Antonellini

and Aydin, 1995; Antonellini and Aydin, 1994; Du Bernard *et al*., 2002; Knott *et al.*, 1996; Fowles and Burley, 1994) fault initiation, propagation and throw accumulation are likely the most significant controlling factors governing the over width of the fault damage zone.

Structural elements in fault damage zones have been shown to act as baffles (Hesthammer *et al.*, 2002) or conduits (Nelson, 2000) to fluid flow in petroleum reservoirs, depending on damage zone end-member type (deformation banded or fractured), and therefore have a significant effect on petroleum asset value. Fault damage zones features are unresolvable using industry standard seismic, gravity and magnetic data, even with the application of geophysical imaging techniques. Also, they are not laterally continuous enough to be fully captured in core data. It is then important to use outcrop analogs to gain an understanding of sub-seismic scale fault damage zone architecture. Data collected and compiled in this study should be used as input for subsurface models at the reservoir scale in order to predict the distribution of sub-seismic fluid-affecting structures in deformation banded and fractured fault damage zones.

6. Appendix: Fault Damage Zone Data

Data in the appendix was collected by the author and David E. Wolf (Structural Geology Research, Shell International Exploration and Production). It is a collection of fault attribute data from several different faults gleaned from literature and this study. Fault throw, damage zone width (hanging wall), structural element density vs distance from the fault core data are compiled here.

Table courtesy David E. Wolf, Structural Geology Research, Shell Intl. E&P

Legend

										Organic rich Lacustrine Limestone
										Dolostone
									Positive = FW	Porcelanite (Dolomitic)
	Not Listed								Negative = HW	Chalk
	Normal Fault									Carbonate
Subsurface	Strike-Slip Fault							Damage Zone Fault	Damage Zone Fault	Mudstone
Field-Based study	Reverse Fault							Background	Background	Crystalline
Reference	Fault type		Fault throw (m)	Damage Zone Width (m)	Damage Zone Width (HW) (m)	Damage Zone Width (FW) (m)	Frac Density (#/m)	Distance from Fault Core (m)	Lithology	
Gilbertown, AL										
Jin & Groshong, 2001, PhD	East Gilbertown Fault (Normal)		122						Eutaw	
			458						Smackover	
			30						Selma Chalk, Subunit 8	
			34.3						Selma Chalk, Subunit 7	
			38.6						Selma Chalk, Subunit 6	
			42.9						Selma Chalk, Subunit 5	
			47.2						Selma Chalk, Subunit 4	
			51.5						Selma Chalk, Subunit 3	
			55.8						Selma Chalk, Subunit 2	
			60						Selma Chalk, Subunit 1	
	East Gilbertown Fault	A-A', 1279	37	46	46	0			Selma Chalk	
		A-A', 2202	46	150	140	10				
		B-B', 3290	23	31	0	31				
		B-B', 75	35	62	31	31				
		B-B', 48	48	51	36	15				
		B-B', 2860	61	30	30	0				
		C-C', 45	31	18	15	3				
		C-C', 54	84	15	15	0				
		D-D', 34	31	31	31	0				
		D-D', 39	37	45	40	5				
		D-D', 40	46	23	23	0				
	E.G.F. Splay	D-D', 4195	23	53	15	38				
Texas										
Zahm et. al. 2010	Normal		2.7914	12.51612903	0.516129032	12			Carbonate	
			5.3467	7.870967742	4	3.870967742				
			6.0864	4.516129032	0.774193548	3.741935484				
			37.072	9.806451613	1.806451613	8				
			3.1235	5.419354839	2.322580645	3.096774194				
			1.4598	5.290322581	1.677419355	3.612903226				
			2.4482	6.193548387	1.806451613	4.387096774				
			1.3716	4	1.677419355	2.322580645				
			25.293	10.19354839	1.935483871	8.258064516				
			5.5977	7.483870968	1.548387097	5.935483871				
			1.5538	5.032258065	1.161290323	3.870967742				
			0.9305	4.258064516	0.774193548	3.483870968				
			1.9182	6.967741935	0.64516129	6.322580645				
			1.6524	3.870967742	1.161290323	2.709677419				
			1.7926	7.096774194	2.967741935	4.129032258				

Utah									
Berg & Skar	Normal Fault			280	210	70			
		Moab Member, Canyon B		67	31	36	8.90		
		Moab Member, Canyon B		75	35	40	6.70		
		Slick Rock Member, Bartlett		82	39	43	3.60		
		Moab Member Hidden Canyon		116	58	58	3.30		
California									
Savage et. al. 2011	Low Tide Fault (Normal)		0.35				2.80	0.83	Silicous Mudstones interbedded with more brittle organic rich mudstones
							2.25	0.61	
							2.88	0.50	
							4.24	0.73	
							2.28	0.38	
							3.85	0.17	
							11.63	0.29	
							21.06	0.24	
							33.68	0.10	
							18.34	0.05	
							53.88	0.08	
							115.18	0.03	
							37.62	0.01	
	Three Mile Fault (Normal)		1.2				2.04	0.29	
							14.30	0.41	
							2.04	0.18	
							8.70	0.24	
							23.52	0.12	
							43.19	0.15	
							100.31	0.15	
							62.72	0.10	
							62.72	0.08	
							43.19	0.07	
	Hackle Fault (Normal)		0.53				7.07	0.25	
							7.07	0.36	
							10.85	0.30	
							15.54	0.20	
							7.07	0.16	
							24.86	0.12	
							15.98	0.08	
							42.60	0.06	
							96.24	0.04	
							43.19	0.03	
							78.23	0.01	
California (Monterey)									
							48.89215	0.027442	Porcelanite (Dolomitized)
							62.75237	0.047046	
							131.82212	0.095428	
							50.84037	0.123721	
							103.63981	0.162720	

Eichhubl & Boles 1998	Normal						87.59284	0.186106
							65.15935	0.213406
							55.25820	0.237884
							53.23231	0.258238
							37.29014	0.270267
							129.40417	0.328540
							39.45149	0.328540
							39.45149	0.393295
							108.73250	0.354440
							54.66381	0.407706
							54.08207	0.451568
							53.23231	0.503379
							25.93138	0.503379
							30.13836	0.564893
							64.27241	0.836849
							51.02639	0.581079
							35.35330	0.626407
							47.70962	0.639980
							34.75299	0.671735
							38.57343	0.772645
							34.75299	0.814191
							34.75299	0.766195
							23.32957	0.717063
							21.78376	0.853035
							21.78376	0.959877
							25.28944	1.228603
							70.96583	1.374301
							18.44154	1.196231
							13.54927	1.115289
							11.89313	1.034347
							15.62153	1.264217
							28.45916	1.380773
							22.01892	1.455242
							18.27629	1.358114
							25.28944	1.490856
							20.07174	1.529701
							13.37192	1.584743
							17.05576	1.681871
							11.05636	1.892324
							15.74168	1.701299
							11.23892	1.821096
							6.44939	2.005638
							12.39820	2.254936
							7.60117	2.190180
							12.62822	2.352064
							24.38349	2.416820
							15.50279	2.462148
							41.03624	2.426534
							24.67851	2.588406
							18.27629	2.737346
							14.20903	2.649932
							16.24224	2.562506
							8.89115	2.844188
							16.63929	2.769718
							10.02564	2.993116
							22.42235	3.043868
							22.42235	3.233086
							29.34203	3.074477
							40.97455	3.110653
							40.97455	3.157954
							139.68285	3.113432
							30.86591	3.199699
							74.24306	3.138472
							11.82559	3.288745

Eichhubl & Boles 1998						9.35820	3.411178	
						14.31862	3.497445	
						19.32403	3.539178	
						20.70303	3.614310	
						13.50533	3.614310	
						10.11476	3.761793	
						15.53533	3.845271	
						40.27825	3.912056	
						50.56173	3.995534	
						28.98323	4.026153	
						33.47267	3.984408	
						28.63447	3.948232	
						28.63447	3.889794	
						15.13958	4.076233	
						6.15817	4.323888	
						15.04387	4.151364	
						16.73869	4.290501	
						15.43456	4.207023	
						2.52312	5.447151	
						2.43413	5.235793	
						2.23782	4.618944	
	Normal					30.65	0.834269	Dolostone
						22.83	3.086892	
						27.84	0.566099	
						16.60	2.336018	
						21.84	0.700184	
						13.15	2.738272	
						10.74	2.175116	
						10.74	0.861086	
						8.61	2.791906	
						25.94	5.500418	
						11.29	2.899174	
						9.90	3.328245	
						9.12	3.328245	
						7.02	0.485648	
						6.02	0.995170	
						5.80	0.270738	
						6.33	1.941497	
						5.13	0.228455	
						6.11	2.427944	
						5.89	2.745132	
						5.05	1.814646	
						4.79	3.400838	
						4.48	1.582025	
						4.92	1.053295	
						4.92	1.624308	
						3.71	3.718026	
						5.01	4.162190	
						4.80	3.845001	
						4.66	6.996180	
						4.07	6.403962	
						3.68	6.763559	
						3.79	7.397935	
						7.76	6.319395	
						6.39	7.545990	
						8.26	6.065570	
						10.28	6.869330	
						8.48	5.769461	
						16.41	8.074720	
						8.33	5.515760	
						10.62	5.938719	
						11.58	5.473476	
						13.44	6.044490	
						9.57	14.165660	
						4.46	13.806189	

						5.23	14.334919	
						19.38	16.513329	
						23.96	17.253476	
						23.96	18.141803	
						5.55	16.090244	
						17.78	18.289858	
						6.78	17.655356	
						13.92	18.205166	
						6.50	17.401531	
						5.45	16.534408	
						4.20	16.069165	
						4.02	15.667285	
						3.80	15.667285	
						4.20	18.141803	
						3.72	17.718719	
						5.11	18.712817	
						5.94	18.268654	
						7.79	19.749074	
						6.57	20.552710	
						15.01	19.643303	
						13.24	21.561526	
						3.09	20.845326	
						5.07	21.375928	
						20.21	21.375928	
						30.72	21.375928	
						2.96	19.916961	
						2.69	20.500572	
						7.15	29.943382	
						9.43	31.747102	
						11.05	33.338657	
						6.48	32.224569	
						4.99	30.500426	
						5.43	34.638344	
						3.68	33.259079	
						3.47	32.383724	
						3.37	33.524255	
						2.61	30.977892	
						2.93	34.479188	
						3.18	36.442064	
						3.60	37.821329	
						3.96	37.821329	
						3.06	37.370430	
						2.50	36.574652	
						2.50	35.805442	
						2.42	34.930087	
						2.23	19.154611	
Atacama, Chile								
	Blanca Fault (Strike-Slip)	35	18			4.45	13.51	Isotropic Granodiorite
						9.81	13.51	
						22.01	7.66	
						31.16	7.66	
						33.46	7.66	
						37.56	4.98	
						66.34	4.98	
						66.34	0.34	
						86.62	0.34	
						86.62	4.49	
		5000	149			117.18	-0.15	Granodiorite and foliated diorite/Isotropic Diorite
						50.81	6.93	
						75.13	15.71	
						44.86	21.81	

Faulkner 2010	Caleta Coloso Fault (Strike-Slip)					64.60	26.68	
						42.53	34.24	
						58.06	43.02	
						38.92	52.54	
						34.36	59.85	
						34.36	68.39	
						40.33	81.07	
						55.53	81.07	
						82.12	91.81	
						90.55	95.95	
						90.55	111.32	
						90.55	128.15	
						68.74	134.98	
						51.27	140.83	
						8.21	140.83	
						4.86	149.37	
						31.16	68.15	
						1.98	18.63	
						2.20	18.63	
	Cristales Fault (Strike-Slip)	200	115			96.37	8.88	Diorite/Isotropic Granodiorite
						55.53	18.63	
						61.79	24.73	
						61.79	30.59	
						28.01	38.63	
						49.47	45.71	
						42.91	54.73	
						32.29	62.29	
						77.85	70.10	
						62.89	82.54	
						62.89	89.85	
						98.10	99.37	
	Strike-Slip	0.1043	0.346151					
		0.9575	0.346151					
		1.5769	0.346151					
		28.167	22.7690788					
		175.47	110.995201					
		4135.4	148.8576126					
	Fault C1 Micro Frac					29.84	0.00	
						26.02	0.00	
						22.12	0.00	
						20.98	0.00	
						20.98	0.01	
						18.75	0.00	
						19.05	0.00	
						19.05	0.01	
						18.75	0.01	
						18.32	0.01	
						17.13	0.01	
						16.10	0.01	
						13.69	0.01	
						18.87	0.01	
						14.80	0.01	
						14.80	0.01	
						14.03	0.01	
						12.05	0.01	
						13.02	0.01	
						12.01	0.02	
						13.69	0.02	
						10.21	0.03	
						8.50	0.03	
						6.79	0.02	
						6.79	0.03	

Mitchell & Faulkner 2009/Faulkner 2010 (Grain scale microfracture measurements #/mm)								
						10.28	0.04	
						6.85	0.04	
						8.55	0.05	
						8.55	0.05	
						8.55	0.05	
						6.81	0.05	
						5.13	0.03	
						5.13	0.03	
						5.13	0.04	
						5.13	0.04	
						5.13	0.05	
						5.76	0.06	
						6.85	0.06	
						6.81	0.06	
						6.81	0.08	
						3.41	0.08	
						3.41	0.08	
						3.05	0.07	
						3.42	0.06	
						3.42	0.05	
						3.61	0.04	
						3.37	0.04	
						3.37	0.04	
						37.52	0.00	
						32.65	0.00	
						32.65	0.00	
						32.65	0.00	
						34.16	0.00	
						27.37	0.00	
						25.77	0.00	
						24.09	0.00	
						20.58	0.00	
						20.58	0.00	
						17.12	0.01	
						17.12	0.01	
						15.47	0.01	
						16.99	0.01	
						20.50	0.01	
						15.29	0.01	
						15.29	0.01	
						13.66	0.01	
						13.66	0.01	
						11.94	0.01	
						10.23	0.01	
						10.23	0.01	
						10.23	0.01	
						10.23	0.02	
						10.23	0.02	
						10.23	0.02	
						11.89	0.01	
						11.89	0.02	
						11.89	0.02	
						11.89	0.02	
						11.89	0.02	
						11.89	0.03	
						13.72	0.05	
						11.94	0.05	
						8.55	0.06	
						8.55	0.05	
						8.55	0.04	
						8.55	0.04	
						8.55	0.04	
						8.55	0.03	
						8.55	0.03	

	Fault FC-13 Micro Frac						8.55	0.03
							8.55	0.02
							8.55	0.02
							8.55	0.02
							8.55	0.02
							8.55	0.01
							8.55	0.01
							6.87	0.01
							6.87	0.02
							6.87	0.03
							6.87	0.03
							6.87	0.03
							6.87	0.04
							6.87	0.04
							6.87	0.04
							6.87	0.04
							6.87	0.05
							6.87	0.05
							6.87	0.05
							6.87	0.05
							6.87	0.05
							6.87	0.06
							6.87	0.06
							6.87	0.07
							5.15	0.03
							5.15	0.04
							5.15	0.04
							5.15	0.04
							5.15	0.05
							5.15	0.05
							5.15	0.05
							5.15	0.05
							5.15	0.05
							5.15	0.05
							5.15	0.05
							5.15	0.06
							5.15	0.06
							5.15	0.07
	Fault FC2-8 Micro Frac						23.95	0.00
							22.32	0.01
							20.49	0.01
							11.96	0.01
							15.39	0.02
							13.72	0.02
							17.21	0.04
							13.67	0.04
							13.67	0.04
							8.56	0.03
							6.82	0.04
							6.82	0.03
							10.27	0.04
							5.11	0.04
	Blanca Fault Micro Frac						4.57	17.73
							5.18	12.77
							5.48	12.77
							5.48	18.20
							6.18	7.81
							6.69	4.97
							6.97	4.97
							7.30	4.97
							7.61	7.81
							8.29	2.37
							8.78	5.21
							9.50	3.32

						9.90	-0.46	
						10.09	3.32	
						13.85	3.08	
						15.11	-0.23	
						15.92	0.72	
	Cristales Fault Micro Frac					18.20	12.70	
						30.49	10.48	
						24.11	6.95	
						38.05	7.41	
						45.37	8.14	
						54.35	15.34	
						61.44	9.68	
						89.56	6.07	
						99.01	3.61	
	Caleta Coloso Fault Micro Frac					15.84	15.39	
						21.51	16.29	
						35.21	11.39	
						40.88	10.09	
						54.59	12.80	
						48.92	8.61	
						59.31	7.41	
						64.28	4.99	
						70.18	7.32	
						77.03	8.65	
						88.85	6.42	
						101.84	9.29	
						106.81	7.49	
						119.09	6.11	
						131.85	4.42	
						138.94	3.47	
						125.94	3.04	
Yemen								
Le Garzic et al	Normal Fault	1000	80	50	20			Crystalline
France								
Matonti et al	Normal Fault	5	21					Carbonate
Italy								
Micarelli et. al. 2006	Normal	0.098	0.39222					Porous Carbonate
		0.4364	0.53228					
		0.098	0.65484					
		0.8088	0.84744					
		0.1995	1.0576					
		1.2149	1.0576					
		0.7073	1.5128					
		1.7904	1.828					
		0.9442	2.4934					
		1.1811	2.4934					
		1.418	2.4934					
		1.9935	3.0011					
		3.9905	2.8085					
		6.0214	3.0011					
		7.1384	3.2113					
		7.9507	3.4039					
		9.9816	2.4233					
		12.012	3.5264					
		14.991	3.9992					
		15.973	3.7015					
		20.001	4.8046					
		30.02	3.719					

New Mexico								
This Study	Normal Fault	450		99		17.00	1.00	Organic rich Lacustrine Limestone
						11.00	2.00	
						11.00	3.00	
						8.00	4.00	
						4.00	5.00	
						8.00	6.00	
						9.00	7.00	
						13.00	8.00	
						8.00	9.00	
						4.00	10.00	
						6.00	11.00	
						13.00	12.00	
						6.00	13.00	
						3.00	14.00	
						8.00	15.00	
						7.00	16.00	
						7.00	17.00	
						6.00	18.00	
						8.00	19.00	
						3.00	20.00	
						5.00	21.00	
						5.00	22.00	
						3.00	23.00	
						7.00	80.00	
							81.00	
							82.00	
							83.00	
						10.00	84.00	
							85.00	
							86.00	
							87.00	
							88.00	
						7.00	89.00	
							90.00	
							91.00	
							92.00	
							93.00	
						8.00	94.00	
						8.00	95.00	
						8.00	96.00	
						8.00	97.00	
						6.00	98.00	
						6.00	99.00	
						3.00	100.00	
						2.00	101.00	
						3.00	102.00	

7. References

Aldrich, M.J., Jr and Dethier, D.P., 1990, Stratigraphic and tectonic evolution of the northern Espanola basin, Rio Grande Rift, New Mexico: Geological Society of America Bulletin, v. 102, p. 1695-1705.

Antonellini, M., Aydin, A., 1994, Effect of faulting of fluid flow in porous sandstone: Petrophysical Properties, AAPG Bulletin. vol. 72, no. 3. p. 355-377.

Aydin, A., Borja, R. I., Eichhubl, P., 2006, Geological and mathematical framework for failure modes in granular rock, Journal of Structural Geology, vol. 28, p. 83-98.

Aydin, A., Johnson, A.M., 1978. Development of faults as zones of deformation bands and as slip surfaces in sandstone. Pure and Applied Geophysics 116, 931–942.

Beach, A., Welbon, A. I., Brockbank, P. J. & McCallum, J. E., 1999, Reservoir damage around faults: outcrop examples from the Suez rift. Petroleum Geoscience, 5(2), 109-116.

Berg, R.R., 1962, Mountain flank thrusting in Rock Mountain foreland, Wyoming and Colorado: American Association of Petroleum Geologists Bulletin, v. 46, p. 2019-2032.

Berglof, W. R. and McLemore, V. T., 2003, Economic geology of the Todilto Formation, New Mexico Geological Society, Guidebook, 54th Field Conference, Geology of the Zuni Plateau, p. 179-189.

Billi, A., Salvini, F., Storti, F., 2003. The damage zone fault core transition in carbonate rocks: implications for fault growth, structure and permeability. Journal of Structural Geology 25, p. 1779-1794.

Braathen, A., Tveranger, J., Fossen, H., Skar, T., Cardozo, N., Semshaug, E., Bastesen, E., Sverdrup, E., 2009, Fault facies and its application to sandstone reservoirs, AAPG Bulletin, Vol. 93, No. 7, pgs. 891-917.

Brace, W.F., Martin, R.J., 1968. A test of law of effective stress for crystalline rocks of low porosity. International Journal of Rock Mechanics and Mining Sciences 5 (5), 415.

Brace,W.F., Paulding, B.W., Scholz, C., 1966. Dilatancy in fracture of crystalline rocks. Journal of Geophysical Research 71 (16), 3939.

Brister, B.S., and Gries, R.R., 1994, Tertiary stratigraphy and tectonic development of the Alamosa Basin (northern San Luis Basin), Rio Grande Rift, south-central Colorado: Geological Society of America Special Paper 291, p. 39-58.

Cather, S.M., 2004, Laramide Orogeny in central and northern New Mexico and southern Colorado, in Mack, G.H. and Giles, K.A., eds., Geology of New Mexico, a geologic history: New Mexico Geological Society Special Publication 11, p. 203-248.

Cather, S.M., Karlstrom, K.E., Timmons, J.M., and Heizler, M.T., 2006, Palinspastic reconstruction of Proterozoic basement-related aeromagnetic features in north-central New Mexico: Implications for Mesoproterozoic to late Cenozoic tectonism: Geosphere, v. 2, p. 299-323.

Chapin, C.E. and Cather, S.M., 1994, Tectonic setting of the axial basins of the northern and central Rio Grande Rift, in Keller, G.R. and Cather, S.M., eds., Basins of the Rio Grande Rift: Structure, Stratigraphy, and Tectonic Setting: Geological Society of America Special Paper 291.

Chapin, C. E., & Seager, W. R. (1975). Evolution of the Rio Grande rift in the Socorro and Las Cruces areas. In *Field Conf. Guideb. NM Geol. Soc* (Vol. 26, pp. 297-321).

Chester, F.M., Chester, J.S., Kirschner, D.L., Schulz, S.E., Evans, J.P., 2004. Structure of large-displacement, strike-slip fault zones. In: Karner, G.D., Taylor, B., Driscoll, N.W., Kohlstedt, D.L. (Eds.), Rheology and Deformation in the Lithosphere at Continental Margins. Columbia Univ. Press, New York.

Church, F.S., and Hack, J.T., 1939, An exhumed erosion surface in the Jemez Mountains, New Mexico: Journal of Geology, v. 47, p. 613–629.

Coney, P.J., 1972, Cordilleran tectonics and North American plate motion: American Journal of Science, v. 272, p. 603-628.

Cowie, P.A., Scholz, C.H., 1992. Physical explanation for the displacement length relationship of faults using a post-yield fracture-mechanics model. Journal of Structural Geology 14 (10), 1133–1148.

DeCelles, P.G., 2004, Late Jurassic to Eocene evolution of the Cordilleran thrust belt and foreland basin system, western U.S.A.: American Journal of Science, v. 304, p. 105-168.

Dickinson, W.R., Klute, M.A., Hayes, M.J., Janecke, S.U., Lundin, E.R., McKittrick, M.A., and Olivares, M.D., 1988, Paleogeographic and paleotectonic setting of Laramide sedimentary basins in the central Rock Mountain region: Geological Society of America Bulletin, v. 100, p. 1023-1039.

Dickinson, W.R., and Snyder, W.S., 1978, Plate tectonics of the Laramide Orogeny, in Mathews, V., III, ed., Laramide folding associated with basement block faulting in the western United States: Geological Society of America Memoir 151, p. 355-366.

Doughty, P.T., 2003. Clay smear seals and fault sealing potential of an exhumed growth fault, Rio Grande Rift, New Mexico. American Association of Petroleum Geologists Bulletin 87 (3), 427–444.

Du Bernard, X., Labaume, P., Darcel, C., Davy, P. and Bour, O., 2002, Clastic slip band distribution in normal fault damage zones, Nubian Sandstones, Suez Rift, Journal of Geophysical Research. vol 107, no. B7, 2141.

Eichhubl, P., & Boles, J. R. (1998). Vein formation in relation to burial diagenesis in the Miocene Monterey Formation, Arroyo Burro Beach, Santa Barbara, California.

Engelder, J.T., 1974. Cataclasis and generation of fault gouge. Geological Society of America Bulletin 85 (10), 1515–1522.

Faulkner, D., Jackson, C., Lunn, R., Schlische, R., Shipton, Z., Wibberley, C., Withjack, M., 2010, A review of recent developments concerning the structure, mechanics and fluid flow properties of fault zones, Journal of Structural Geology, 32, pgs. 1557-1575.

Ferrill, D. A., Morris, A. P., McGinnis, R. N., Smart, K. J., & Ward, W. C., 2011, Fault zone deformation and displacement partitioning in mechanically layered carbonates: The Hidden Valley fault, central Texas. AAPG bulletin, 95(8), 1383-1397.

Flodin, E., and Aydin, A., 2004, Faults with asymmetric damage zones in sandstone, Valley of Fire State Park, southern Nevada, Journal of Structural Geology. Vol. 26, p. 983-988.

Fossen, H. (2010). Structural geology. Textbook. Cambridge University Press.

Fossen, H., Schultz, R., Shipton, Z., Mair, K., 2007, Deformation bands in sandstone: a review, Journal of the Geological Society of London, Vol. 164, pgs. 755-769.

Fowles, J. and Burley, S., 1994, Textural and permeability characteristics of faulted, high porosity sandstones, Mar. Pet. Geol., 11, 608– 623. Garfunkel, Z., and Y. Bartov, The tectonics of Suez rift, Bull. Geol. Surv., 71, 1977.

Gonzalez, M.A., and Dethier, D.P., 1991, Geomorphic and neotectonic evolution along the margin of the Colorado Plateau and Rio Grande rift, northern New Mexico, *in* Julian, B., and Zidek, J., eds., Field guide to geologic excursions in New Mexico and adjacent areas of Texas and Colorado: New Mexico Bureau of Mines and Mineral Resources Bulletin 137, p. 29-45.

Ingersoll, R.V., 2001, Structural and stratigraphic evolution of the Rio Grande Rift, northern New Mexico and southern Colorado: International Geology Review, v. 43, p. 867-891.

Hamilton, J.S., 2009, A new multistage model for the Late Mesozoic to present tectonic evolution of north-central New Mexico (Master's thesis): University of Houston, Houston, Texas, 84 p.

Healy, D., Jones, R.R., Holdsworth, R.E., 2006. Three-dimensional brittle shear fracturing by tensile crack interaction. Nature 439 (7072), 64–67.

Hicks, R.T., 2008, Structural evolution of the Cañones fault system portion of the Rio Grande Rift: Implications for the development of transfer zones (Master's thesis): University of Houston, Houston, Texas, 70 p.

Ingersoll, R.V., 2001, Structural and stratigraphic evolution of the Rio Grande Rift, northern New Mexico and southern Colorado: International Geology Review, v. 43, p. 867-891.

Karlstrom, K.E., and Daniel, C.G., 1993, Restoration of Laramide right-lateral strike-slip in northern New Mexico by using Proterozoic piercing points: Tectonic implications from the Proterozoic to the Cenozoic: Geology, v. 21, p. 1139-1142.

Karlstrom, K. E., Cather, S. M., Kelly, S. A., Heizler, M. T., Pazzaglia, F. J. and Roy, M., 1999, Sandia Mountains and Rio Grande Rift: Ancestry of structures and history of deformation, New Mexico Geological Society, Guidebook, 50th Field Conference, Albuquerque Geology.

Kelley, S.A., Osburn, G.R., Ferguson, C., Moore, J., Kempter, K. 2005, Preliminary geologic map of the Cañones 7.5-minute quadrangle, Rio Arriba County, New Mexico, New Mexico Bureau of Geology and Mineral Resources, Open-file Geologic Map OF-GM 107, scale 1:24,000.

Kempter, K., Zeigler, K., Koning, D., and Lucas, S., 2007, Preliminary geologic map of the Canjilon SE quadrangle, Rio Arriba County, New Mexico: New Mexico Bureau of Geology and Mineral Resources, Open-file Geologic Map and Report, v. 150, 1:24,000.

Kim, Y.S., Peacock, D.C.P., Sanderson, D.J., 2004. Fault damage zones. Journal of Structural Geology 26 (3), 503–517.

Knott, S.D., Beach, A., Brockbank, P.J., Brown, J.L., McCallum, J.E., Welbon, A.I., 1996. Spatial and mechanical controls on normal fault populations. Journal of Structural Geology 18 (2-3), 359–372.

Ladeira, F. L., & Price, N. J. (1981). Relationship between fracture spacing and bed thickness. Journal of Structural Geology, 3(2), 179-183.

Le Garzic, E., de L'Hamaide, T., Diraison, M., Géraud, Y., Sausse, J., De Urreiztieta, M. and Champanhet, J. M., 2011, Scaling and geometric properties of extensional fracture

systems in the proterozoic basement of Yemen. Tectonic interpretation and fluid flow implications. Journal of Structural Geology, 33(4), 519-536.

Lindanger, M. Roy H. Gabrielsen & Alvar Braathen. Analysis of rock lenses in extensional faults. *Norwegian Journal of Geology,* vol. 87, pp. 361-372.

Lockner, D.A., Byerlee, J.D., Kuksenko, V., Ponomarev, A., Sidorin, A., 1991. Quasi-static fault growth and shear fracture energy in granite. Nature 350 (6313), 39–42.

Lucas, S.G., 1993, The Chinle Group—Revised stratigraphy and biochronology of Upper Triassic strata in the western United States: Museum of Northern Arizona Bulletin, v. 59, p. 27–50.

Lucas,S.G., and Krainer, K., 2005, Stratigraphy and correlation of the Permo-Carboniferous Cutler Group, Chama Basin, New Mexico: New Mexico Geological Society, Guidebook 56, p. 145-159.

Lucas, S.G., Hunt, A.P., and Spielmann,J., 2005, Jurassic stratigraphy in the Chama Basin, northern New Mexico: New Mexico Geological Society, Guidebook 56, p. 182-192.

Lucas, S. G., Kietzke, K. K. and Hunt, A. P., 1985, The Jurassic system in east-central New Mexico: New Mexico Geological Society, Guidebook 36, p. 213–242.

Magnani, M. B., Miller, K. C., Levander, A., Karlstrom, K., 2004, The Yavapai-Mazatzal boundary: A long lived tectonic element in the lithosphere of southwest North America, Geological Society of America Bulletin. V. 116, no. 7/8.

Maldonado, F., and Kelley, S,A., 2009, Revisions to the stratigraphic nomenclature of the Abiquiu Formation, Abiquiu and contiguous areas, north-central New Mexico: New Mexico Geology, v. 31, p. 3-8.

Manly, K., 1984, Brief summary of the Tertiary geologic history of the Rio Grande Rift in northern New Mexico: New Mexico Geological Society, Guidebook. 35, p. 63-66.

Manley, K. and Mehnert, H.H., 1981, New K-Ar ages for Miocene and Pliocene volcanic rocks in the northwestern Española basin and their relationships to the history of the Rio Grande rift: Isochron West, v. 30, p. 5–8.

Matonti, C., Lamarche, J., Guglielmi, Y. and Marié, L., 2012, Structural and petrophysical characterization of mixed conduit/seal fault zones in carbonates: Example from the Castellas fault (SE France). Journal of Structural Geology, 39, 103-121.

McQuillan, H. "Small-scale fracture density in Asmari Formation of southwest Iran and its relation to bed thickness and structural setting." AAPG Bulletin 57.12 (1973): 2367-2385.

Micarelli, L., Benedicto, A., Wibberley, C., 2006, Structural evolution and permeability of normal fault zones in highly porous carbonate rocks, Journal of Structural Geology, 28, pgs. 1214-1227.

Mitchell, T., Faulkner, D., 2009, The nature and origin of off-fault damage surrounding strike-slip fault zones with a wide range of displacements: A field study from the Atacama fault system, northern Chile, Journal of Structural Geology, 31, pgs. 800-816.

Moore, J. D., 2000, Tectonics and volcanism during deposition of the Oligocene-Lower Miocene Abiquiu Formation in Northern New Mexico [MS Thesis]: Albuquerque, University of New Mexico, 144 p.

Nelson, E.P., Kullman, A.J., Gardner, M.H., 1999. Fault-fracture networks and related fluid flow and sealing, Brushy Canyon Formation, West Texas. In: Goodwin, L.B., Mozley, P.S., Moore, J.M., Haneberg, W.C. (Eds.), Faults and Subsurface Fluid Flow in the Shallow Crust Geophysical Monograph 113. American Geophysical Union, Washington, p. 69–81.

Palchik, V., 1999. Influence of porosity and elastic modulus non-uniaxial compressive strength in soft brittle porous sandstones. Rock Mechanics & Rock Engineering, 32, pgs. 303-309.

Palchik, V., 2006. Application of Mohr–Coulomb failure theory to very porous sandy shales, International Journal of Rock Mechanics & Mining Sciences, 43(7), 1153-1162.

Paterson, M.S., Wong, T.-F., 2005. Experimental Rock Deformation; the Brittle Field. Springer-Verlag, Berlin, Heidelberg, New York, 348 pp.

Peng, S., Johnson, A.M., 1972. Crack growth and faulting in cylindrical specimens of Chelmsford granite. International Journal of Rock Mechanics and Mining Sciences 9 (1), 37.

Savage, H., Brodsky, E., 2010, Collateral damage: Evolution with displacement of fracture distribution and secondary fault strands in fault damage zones, Journal of Geophysical Research, Vol. 116, BO3405.

Schueller, S., Braathen, A., Fossen, H. and Tveranger, J., 2013, Spatial distribution of deformation bands in damage zones of extensional faultsin porous sandstones: Statistical analysis of field data, Journal of Structural Geology, vol. 52, p. 148-162.

Shaffer, W.L., 1970, Tectonics of the Rio Grande depression, New Mexico: Unpublished open-file report, University of New Mexico, 18.

Shipton, Z.K. & Cowie, P.A. 2001. Analysis of three-dimensional damage zone development over _m to km scale range in the high-porosity Navajo sandstone, Utah. Journal of Structural Geology, 23, 1825–1844.

Shipton, Z.K. & Cowie, P.A. 2003. A conceptual model for the origin of fault damage zone structures in high-porosity sandstone. Journal of Structural Geology, 25, 333–345.

Scholz, C.H., Aviles, C.A., 1986. The fractal geometry of faults and faulting. In: Das, S., Boatwright, J., Scholz, C. (Eds.), Earthquake Source Mechanics. Academic Press, New York, p. 9.

Scholz, C.H., Dawers, N.H., Yu, J.Z., Anders, M.H., 1993. Fault growth and fault scaling laws – preliminary-results. Journal of Geophysical Research – Solid Earth 98 (B12), 21951–21961.

Scholz, C.H., Lawler, T.M., 2004. Slip tapers at the tips of faults and earthquake ruptures. Geophysical Research Letters 31 (21).

Smith, G. A., Moore, J. D. and Mclntosh, W. C., 2002, Assessing roles of volcanism and basin subsidence in causing Oligocene-Lower Miocene sedimentation in the northern Rio Grande Rift, New Mexico, USA: Journal of Sedimentary Research. vol. 72, p. 836-848.

Smith, H.T.U., 1938, Tertiary geology of the Abiquiu quadrangle, Rio Arriba County, New Mexico: Journal of Geology, v. 46, p. 933–965.

Spieker, E.M., 1946, Late Mesozoic and early Cenozoic history of central Utah: U.S. Geological Survey Professional Paper 205-D, p. 117-161.

Tondi, E., Antonellini, M., Aydin, A., Marchegiani, L., Cello, G., 2006, The role of deformation bands, stylolites and sheared stylolites in fault development in carbonate grainstones of Majella Mountain, Italy, Journal of Structural Geology, 28, pgs. 376-391.

Torabi, A., Fossen, H., & Braathen, A., 2013, Insight into petrophysical properties of deformed sandstone reservoirs. AAPG bulletin, 97(4), 619-637.

Tweto, O., 1975, Laramide (Late Cretaceous-early Tertiary) Orogeny in the southern Rocky Mountains, in Curtis, B.F., ed., Cenozoic history of the southern Rocky Mountains: Geological Society of America Memoir 144, p. 1-44.

Vazzana, M.E., and Ingersoll, R.V., 1981, Stratigraphy, sedimentology, petrology, and basin evolution of the Abiquiu Formation (Oligo-Miocene), north-central New Mexico: Summary: Geological Society of America Bulletin, v. 92, p. 990-992.

Woodward, L.A., 1974, Tectonics of central-northern New Mexico: New Mexico Geological Society, Guidebook 25, p. 123-129.

Woodward, L.A., 1987, Geology and mineral resources of Sierra Nacimiento and vicinity, New Mexico: New Mexico Institute of Mining and Technology Memoir 42, 85p.

Wu, H. and Pollard, D., 1995, An experimental study of the relationship between joint spacing and layer thickness. Journal of Structural Geology, 17(6), 887-905.

Yin, A., and Ingersoll, R.V., 1997, A model for evolution of Laramide axial basins in the southern Rocky Mountains, USA: International Geology Review, v. 39, p. 1113-1123.